

Two Localization Strategies for Sequential MCMC Data Assimilation with Applications to Nonlinear Non-Gaussian Geophysical Models

Hamza Ruzayqat¹, Hristo G. Chipilski², and Omar Knio¹

¹Applied Mathematics and Computational Science Program,
Computer, Electrical and Mathematical Sciences and Engineering Division,
King Abdullah University of Science and Technology, Thuwal, 23955-6900, KSA.

²Department of Scientific Computing, Florida State University,
400 Dirac Science Library, Tallahassee, FL 32306-4120, USA.

E-Mail: hamza.ruzayqat@kaust.edu.sa, hchipilski@fsu.edu, omar.knio@kaust.edu.sa

Abstract

We present a localized data assimilation (DA) scheme based on the sequential Markov Chain Monte Carlo (SMCMC) technique [49], a provably convergent method for filtering high-dimensional, nonlinear, and potentially non-Gaussian state-space models. Unlike particle filters, which are exact methods for nonlinear non-Gaussian models, SMCMC does not assign weights to samples and therefore avoids weight degeneracy in small-ensemble regimes. We design two localization approaches within the SMCMC framework that exploit spatial sparsity of observations to reduce the effective degrees of freedom and improve efficiency. The first variant collects observed blocks into a single reduced domain and runs parallel MCMC chains over this combined region. The second variant further reduces the per-chain state dimension by decomposing the observed region into independent blocks, each augmented with a compact halo, and applying Gaspari–Cohn observation-noise tapering to smoothly down-weight distant observations. When the observation model is linear and Gaussian, we show that our approximate filtering density reduces to a Gaussian mixture from which independent samples can be drawn exactly. For nonlinear or non-Gaussian observation models, we employ an MCMC kernel. We test on high-dimensional ($d \sim 10^4 - 10^5$) state-space models, including a linear Gaussian model and a nonlinear multilayer shallow water equation with both linear and nonlinear observation operators. We consider Gaussian and non-Gaussian (Student- t) observation noise, showing that LSMCMC naturally handles heavy-tailed errors that cause ensemble Kalman methods to diverge. Observations include synthetic and real data from the Surface Water and Ocean Topography (SWOT) mission (NASA) and ocean drifter data (NOAA). We compare the two variants against each other and the local ensemble transform Kalman filter (LETKF).

Keywords: Ensemble Data Assimilation, Localization, Sequential Markov Chain Monte Carlo, High-Dimensional Filtering, Non-Gaussian Noise, Nonlinear Data Assimilation

MSC classes: 62M20, 60G35, 60J20, 94A12, 93E11, 65C40

Corresponding author: Hamza Ruzayqat. E-mail: hamza.ruzayqat@kaust.edu.sa

Code: <https://github.com/ruzayqat/LSMCMC>

1 Introduction

Data assimilation (DA) plays a crucial role in understanding and predicting complex systems states as accurately as possible. By combining partial, noisy observational data with numerical models, DA aims to predict the conditional probability distribution, or the filter distribution, of underlying hidden state variables that cannot be directly observed. In practice, data assimilation is widely utilized across various fields. In finance, it helps in predicting market trends and managing risks by improving the accuracy of financial models. In engineering, it is used to optimize systems and processes by refining predictions based on real-time data. In geophysical sciences, data assimilation is crucial for applications such as numerical weather prediction, where it provides vital information for forecasting weather patterns, understanding atmospheric conditions, and modeling oceanographic phenomena. These applications are particularly useful for paleoclimate reconstructions, ensuring maritime safety, and predicting natural hazards like tsunamis [41]. For a comprehensive introduction on DA and stochastic filtering see [7, 11, 34, 16]. For a deeper exploration of specific applications and methodologies see [13, 27, 35].

Ensemble methods, such as the ensemble Kalman filter (EnKF) [22, 31, 23] and sequential Monte Carlo methods such as particle filters (PFs) [28, 19, 53], are powerful DA tools that have gained significant attention in recent work; see [54] for a review of DA methods. These probabilistic methods, which can be formalized within a sequential Bayesian inference framework, use multiple ensemble members or particles to represent and propagate the system's state dynamics, in conjunction with the available observations. Despite their inherent computational efficiency and their wide usage, ensemble Kalman methods can be inaccurate when dealing with strongly nonlinear and non-Gaussian models. Additionally, they have a tendency to significantly underestimate

the overall uncertainty in the system in small ensemble regimes [44, 52, 54]. PFs, on the other hand, are exact methods (see e.g. [18]) that assign weights to the ensemble members (also called particles) that reflect the likelihood of the observations. As the number of particles approaches infinity, the PF estimates the conditional distribution of the hidden state exactly, regardless of the type of noise present in the system or whether the underlying dynamical model is linear or non-linear. The computational complexity of PFs is fixed per-time-step update. However, in order to prevent the so-called weight degeneracy (see e.g. [8]), the number of particles must grow exponentially with the dimensionality of the state space. This is the primary limitation of standard PF approaches, as they are typically only practical for low-dimensional problems. Several works in the literature have explored different techniques such as tempering, lagging and nudging to tackle this issue; see e.g. [1, 48, 17, 36].

Another exact method for filtering is Markov chain Monte Carlo (MCMC) [11]. MCMC can be used to sample from the filter distribution, however, its computational complexity grows linearly with time, which makes it impractical for real-time applications. A possible solution to the linear growth of complexity is to use sequential MCMC. At each assimilation time step, one builds an MCMC chain initialized from one random sample at the previous time step. Sequential MCMC has been used in dynamic contexts in several works. For instance, in the work of [51], a sequential MCMC based on Hamiltonian Monte Carlo (HMC) [42] was presented. The authors use HMC to build a chain of N samples from the posterior initialized from a uniformly picked sample from the previous time step. Another example is the work of [12], where the authors use Sequential MCMC for dynamical cluster tracking.

In [49], a more practical filtering approach is presented where sequential MCMC chains are used to target the filter distribution at each time-step update. The method was mainly developed for state-space models (SSMs) with unknown random observational locations, but it can be used for general SSMs. The initial idea behind their scheme first appeared in [9] and was later used for point process filtering in [38]. The authors in [49] demonstrate that when high accuracy is needed and the state dimension is very large, the sequential MCMC filtering scheme (which we refer to as SMCMC from now on) is much more accurate and efficient when compared to ensemble methods. When the forward model noise covariance matrix Q_k (and the observation noise covariance R_k) are dense, evaluating the transition and likelihood densities requires $\mathcal{O}(d^2)$ and $\mathcal{O}((d_y^k)^2)$ operations per sample, respectively, due to the matrix–vector products in the quadratic forms. In many practical applications, Q_k and R_k are diagonal, so the quadratic forms reduce to element-wise operations and the overall cost per update becomes $\mathcal{O}(N_a d)$, where N_a denotes the number of MCMC (analysis) samples and d the state dimension. More generally, if Q_k and R_k possess exploitable structure (e.g. Toeplitz/circulant or block-circulant) for stationary kernels on regular grids, separable Kronecker structure on tensor-product grids, or hierarchical off-diagonal low-rank structure, then matrix–vector products can be carried out in $\mathcal{O}(d \log d)$ (or near-linear) time using FFT-based or hierarchical algorithms, leading to an overall complexity of $\mathcal{O}(N_a d \log d)$ per update.

In many real-world applications, observations on the system are either very sparse in the domain of interest or localized in particular regions. Many localization techniques have been developed in the literature to leverage this, thereby improving the overall performance. In [26], the authors introduced a distance-based tapering function which is compactly supported that can be multiplied by the covariance matrix or its estimation to reduce the influence of observations that are spatially far from the state variables being updated. This type of techniques have been largely used in the literature for improving ensemble methods performance, such as EnKF or ensemble transform Kalman filter; see e.g. [31, 32, 30, 55, 3, 43, 40, 29]. Whereas fixed localization functions have been widely used, it was shown that adaptive localization, which dynamically adjusts the localization radius length scale based on the spatial correlation structure, is very effective in practice, e.g. [4, 5]. Furthermore, localization and adaptive localization have been used in PFs as well. An approach is to apply localization directly to the weights and resampling process aiming to reduce the path degeneracy and improving the effective sample size. Examples are the works of [45, 24], where localization is applied to the particles update ensuring that only observations within a distance influence each particle.

In this work, we build upon the SMCMC approach in [49] and propose two localized variants. Both exploit the spatial sparsity of observations by partitioning the domain into subdomains and restricting the MCMC updates to regions where observations exist, thereby reducing the effective state dimension from d to $d' < d$. Since the main cost of the SMCMC filter comes from evaluating pointwise the transition and likelihood densities, which involves vector-matrix multiplications, both variants dramatically reduce this cost while maintaining high accuracy. The first variant collects all observed subdomains into a combined reduced domain and runs parallel MCMC chains over it. The second variant further reduces the per-chain dimension by decomposing the observed region into independent blocks, each augmented with a compact halo, and applying Gaspari–Cohn observation-noise tapering to smoothly down-weight distant observations. The cost order of the new algorithms is $\mathcal{O}(N_a d')$ with $d' < d$.

The contributions of this article are as follows:

- We introduce two localization techniques for the SMCMC filter based on the sparsity of the observations: (a) a joint localization scheme ([Algorithm 1](#)) that collects all observed subdomains into a single reduced domain and runs parallel MCMC chains over this combined region, and (b) a halo-based per-block localization ([Algorithm 2](#)) that decomposes the problem into independent, fully parallel MCMC chains over each observed block with Gaspari–Cohn observation-noise tapering to smoothly down-weight distant observations; see [Figure 1](#) for an illustration.
- We carefully distinguish between the number of forecast samples N_f and the number of analysis (MCMC) samples N_a , and show that when the observation model is linear and Gaussian, the filtering density is a Gaussian mixture from which N_a independent samples can be drawn exactly without MCMC ([Example 3.1](#)).
- For nonlinear observation models, we employ an MCMC kernel (see [Example 3.2](#)) and MCMC chains are run in parallel.
- We apply the method on several challenging SSMs with both linear and nonlinear observations models, including the nonlinear multilayer shallow water equations. We further demonstrate robustness to non-Gaussian observation noise by employing Cauchy-distributed (Student- t , $\nu=1$) errors, motivated by the heavy-tailed error distributions observed in real ocean drifter data [[20](#)].
- We demonstrate the methodology on filtering problems with two types of observations: (a) synthetic and real data from the SWOT mission led by NASA [[56](#), [46](#)], and (b) real ocean drifter observations from NOAA [[37](#)].

This article is structured as follows. [Section 2](#) describes the class of SSMs considered in this paper. In [Section 3](#) we provide a brief review of the SMCMC filter and discuss the direct Gaussian mixture sampling for linear-Gaussian observation models and the choice of MCMC kernel for nonlinear or non-Gaussian observation models. [Section 4](#) proposes the localization SMCMC algorithm in two variants: a joint scheme and a halo-based per-block scheme with Gaspari–Cohn tapering. In [Section 5](#) we demonstrate the methodology on several SSMs. Finally, in [Section 6](#) we conclude with a summary of key results and a discussion of possible future directions.

2 Preliminaries

Consider a two-dimensional grid \mathbf{G} of size $N_g \in \mathbb{N}$. \mathbf{G} is typically a connected region such as a square or a rectangle with $N_g = N_g^x \times N_g^y$, where $N_g^x, N_g^y \in \mathbb{N}$. Assume there is an unknown continuous time stochastic process $(\mathbf{Z}_t)_{t \geq 0}$, with $\mathbf{Z}_t \in \mathbb{R}^d$, and $d \in \mathbb{N}$ is a multiple of $N_g^x N_g^y$ (depending on the number of prognostic variables defined on each grid point). We will consider noisy observations that are arriving at times, $\mathbb{T} := \{t_1, t_2, \dots\} \subset \mathbb{N}$, $0 < t_1 < t_2 < \dots$, at a collection of known locations. Let $m_k \in \mathbb{N}$ be the number of observed locations at time t_k . Then, at the observed location $j \in \{1, \dots, m_k\}$, the observation is denoted by $Y_{t_k}^{(j)} \in \mathbb{R}^s$, $s \in \mathbb{N}$ the number of observed variables per observational location. We denote by $\mathbf{Y}_{t_k} \in \mathbb{R}^{d_y^k}$, $d_y^k = sm_k$, the collection of observations at time t_k . We have a superscript k attached to d_y to indicate that the number of available observations per assimilation cycle may change from time to time. We will assume the time-lag between two consecutive observations to be $L \in \mathbb{N}$, that is $t_{k+1} - t_k = L$.

The modeling approach for the process \mathbf{Z}_t is based on a continuous-time framework, motivated by applications in atmospheric and ocean sciences. In these domains, physical quantities such as height, wind, or water velocity are described using continuous-time, spatially-varying physical models represented by systems of partial differential equations (PDEs). To account for model uncertainty, the dynamics of \mathbf{Z}_t are modeled using a stochastic process, where the noise can be incorporated either continuously (as in stochastic PDEs) or discretely in time.

The framework requires that at observation times $t_k \in \mathbb{T}$, the process $(\mathbf{Z}_{t_k})_{k \geq 1}$ is Markov with a known, positive transition density $f_k(\mathbf{z}_{t_{k-1}}, \mathbf{z}_{t_k})$. The initial state \mathbf{Z}_0 is assumed known. Each observation \mathbf{Y}_{t_k} depends only on \mathbf{Z}_{t_k} through a positive likelihood density $g_k(\mathbf{z}_{t_k}, \mathbf{y}_{t_k})$. The subscript k in f_k and g_k allows for time-inhomogeneous dynamics or observation processes.

We assume that f_k (or a suitable approximation) can be evaluated pointwise. This includes stochastic differential equations and their time-discretization approximations, stochastic PDEs, or PDEs with discrete-time additive noise. A state-space model that fits this setup and applies to all examples in this article is presented below.

Hidden signal: We will consider \mathbf{Z}_t to be a vector containing hidden state variables at positions defined on G . Let $\Phi : \mathbb{R}^d \times \mathbb{R}_+^2 \rightarrow \mathbb{R}^d$ be some linear or nonlinear function defined on its domain, then for $k \in \mathbb{N}$:

$$\mathbf{Z}_t = \Phi(\mathbf{Z}_{t_{k-1}}, t_{k-1}; t), \quad t \in (t_{k-1}, t_k), \quad (2.1)$$

and at time of observation t_k :

$$\mathbf{Z}_{t_k} = \Phi(\mathbf{Z}_{t_{k-1}}, t_{k-1}; t_k) + \mathbf{W}_{t_k}, \quad (2.2)$$

where $\mathbf{W}_{t_k} \stackrel{i.i.d.}{\sim} \mathcal{N}_d(0, Q_k)$ is an i.i.d. sequence of d -dimensional Gaussian random variables of zero mean and covariance matrix Q_k .

Observations: In addition, the following observational model is considered

$$\mathbf{Y}_{t_k} = \mathcal{O}_{t_k}(\mathbf{Z}_{t_k}) + \mathbf{V}_{t_k}, \quad (2.3)$$

where $\mathcal{O}_{t_k} : \mathbb{R}^d \rightarrow \mathbb{R}^{d_y^k}$ is an $\mathbb{R}^{d_y^k}$ -vector valued function and $\{\mathbf{V}_{t_k}\}$ is an i.i.d. noise sequence with known density. In most experiments, $\mathbf{V}_{t_k} \sim \mathcal{N}_{d_y^k}(0, R_k)$; however, the LSMCMC framework accommodates arbitrary observation noise distributions, and in [Subsection 5.4](#) we consider heavy-tailed Cauchy (t_1) errors to demonstrate this generality.

Throughout this work, we restrict ourselves to the case where both Q_k and R_k are *diagonal* matrices. This is a natural assumption in many applications where the noise components are independent across spatial locations and observed variables. Under this assumption, evaluating the transition density f_k and the likelihood g_k involves only element-wise operations, reducing the per-sample cost of the SMC algorithm to $\mathcal{O}(d + d_y^k)$.

3 SMC Filter

Inference of the hidden state is performed using conditional distributions given the available observations. One can either consider the whole path trajectory $\mathbb{P}(\mathbf{Z}_{t_1}, \dots, \mathbf{Z}_{t_k} | (\mathbf{Y}_{t_p})_{p \leq k})$ (smoothing) or just the marginal $\mathbb{P}(\mathbf{Z}_{t_k} | (\mathbf{Y}_{t_p})_{p \leq k})$ (filtering). For $k \in \mathbb{N}$ we define the smoothing density (the dependence on observations is dropped from the notation)

$$\begin{aligned} \Pi_k(\mathbf{z}_{t_1}, \dots, \mathbf{z}_{t_k}) &\propto \prod_{p=1}^k f_p(\mathbf{z}_{t_{p-1}}, \mathbf{z}_{t_p}) g_p(\mathbf{z}_{t_p}, \mathbf{y}_{t_p}) \\ &\propto f_k(\mathbf{z}_{t_{k-1}}, \mathbf{z}_{t_k}) g_k(\mathbf{z}_{t_k}, \mathbf{y}_{t_k}) \Pi_{k-1}(\mathbf{z}_{t_1, k-1}). \end{aligned} \quad (3.1)$$

Let $\pi_k(\mathbf{z}_{t_k})$ be the marginal in the \mathbf{z}_{t_k} coordinate of the smoothing distribution Π_k . It easily follows that the filter density can be obtained recursively

$$\pi_k(\mathbf{z}_{t_k}) \propto g_k(\mathbf{z}_{t_k}, \mathbf{y}_{t_k}) \int_{\mathbb{R}^d} f_k(\mathbf{z}_{t_{k-1}}, \mathbf{z}_{t_k}) \pi_{k-1}(\mathbf{z}_{t_{k-1}}) d\mathbf{z}_{t_{k-1}}. \quad (3.2)$$

The filtering problem we are considering is inherently discrete-time in nature, as the observations are obtained at discrete time instances. However, we can still obtain the conditional probability distribution $\mathbb{P}(\mathbf{Z}_t | (\mathbf{Y}_{t_p})_{p \leq k})$ for any time $t \in (t_k, t_{k+1})$. This can be achieved by integrating the previous filter distribution π_{k-1} with the corresponding transition density, and then applying the Chapman-Kolmogorov equations. This allows us to propagate the filter distribution continuously in time, even though the observations are discrete.

The method of [\[49\]](#) efficiently approximates [\(3.2\)](#) directly via a sequence of MCMC chains each initialized from a previously obtained approximation of π_{k-1} . At time t_1 their algorithm targets $\pi_1(\mathbf{z}_{t_1})$ exactly by running an MCMC kernel with invariant distribution $\pi_1(\mathbf{z}_{t_1})$ for N_a steps, that is to draw N_a samples from

$$\pi_1(\mathbf{z}_{t_1}) \propto g_1(\mathbf{z}_{t_1}, \mathbf{y}_{t_1}) f_1(\mathbf{Z}_0, \mathbf{z}_{t_1}). \quad (3.3)$$

At later times t_k , $k \geq 2$, the filter distribution π_{k-1} is approximated by an empirical measure constructed from N_f forecast samples carried over from the previous step. In the original SMC algorithm of [\[49\]](#), all N_a samples from the previous MCMC chain serve as forecast samples, i.e., $N_f = N_a$. We introduce a simple but effective modification: we retain only a subset of $N_f \leq N_a$ samples for the forecast step. This decoupling is motivated by the observation that, during the MCMC chain at each cycle, the auxiliary ancestor index j (see [\(3.4\)](#) and [\(3.5\)](#) below) selects among the N_f previous samples, and many MCMC iterates may re-use the same index, so

only a fraction of the forecast samples actually influence the posterior. Keeping N_f small therefore economizes on the forecast step—which requires running the forward model N_f times—while still allowing a long MCMC chain ($N_a \gg N_f$) to thoroughly explore the posterior. This is particularly beneficial when the forward model is computationally expensive.

Concretely, the empirical measure of the N_f forecast samples is $S_{k-1}^{N_f}(\mathbf{z}_{t_{k-1}}) := \frac{1}{N_f} \sum_{i=1}^{N_f} \delta_{\{\mathbf{z}_{t_{k-1}}^{(i)}\}}(\mathbf{z}_{t_{k-1}})$, where $\delta_{\{\mathbf{z}_{t_k}\}}(\mathbf{z})$ denotes the Dirac delta measure centered at \mathbf{z}_{t_k} . Substituting $S_{k-1}^{N_f}$ into (3.2) yields the approximate filtering density

$$\pi_k^{N_f}(\mathbf{z}_{t_k}) \propto g_k(\mathbf{z}_{t_k}, \mathbf{y}_{t_k}) \frac{1}{N_f} \sum_{j=1}^{N_f} f_k(\mathbf{z}_{t_{k-1}}^{(j)}, \mathbf{z}_{t_k}). \quad (3.4)$$

This density is the marginal of the joint distribution

$$\pi_k^{N_f}(\mathbf{z}_{t_k}, j) \propto g_k(\mathbf{z}_{t_k}, \mathbf{y}_{t_k}) f_k(\mathbf{z}_{t_{k-1}}^{(j)}, \mathbf{z}_{t_k}) p(j), \quad (3.5)$$

where $j \in \{1, \dots, N_f\}$ is an auxiliary ancestor index with uniform prior $p(j) = 1/N_f$. The SMCMC algorithm then draws N_a samples from $\pi_k^{N_f}(\mathbf{z}_{t_k}, j)$ using an MCMC kernel, with $N_a \geq N_f$.

For a given function $\varphi : \mathbb{R}^d \rightarrow \mathbb{R}$ that is π_k -integrable, one is interested in estimating expectations w.r.t. the filtering distribution at observation times $(t_k)_{k \geq 1}$. These expectations are given by $\pi_k(\varphi) := \int_{\mathbb{R}^d} \varphi(\mathbf{z}_{t_k}) \pi_k(\mathbf{z}_{t_k}) d\mathbf{z}_{t_k}$. After obtaining N_a samples from $\pi_k^{N_f}$ in (3.5), the expectation $\pi_k(\varphi)$ can be estimated through $\hat{\pi}_k^{N_a}(\varphi) := \frac{1}{N_a} \sum_{i=1}^{N_a} \varphi(\mathbf{Z}_{t_k}^{(i)})$, which as $N_a \rightarrow \infty$ converges to the true expectation $\pi_k(\varphi)$ almost surely [49].

Choice of MCMC Kernel

The choice of the MCMC kernel used to sample from $\pi_k^{N_f}$ in (3.5) (or its localized version (4.3)) depends critically on the structure of the observation model \mathcal{O}_{t_k} . We describe two important cases below.

We emphasize that when the observation model is linear and Gaussian, the filtering density takes the form of a Gaussian mixture from which N_a independent samples can be drawn directly without any MCMC iterations, as shown in the following example. This observation, which was not exploited in the original SMCMC framework of [49], eliminates burn-in and inter-sample correlation in this important special case.

Example 3.1 (Linear-Gaussian observation model – direct sampling). *Consider the SSM (2.2)–(2.3) with a linear observation operator $\mathcal{O}_{t_k}(\mathbf{z}) = C\mathbf{z}$ and Gaussian noises in both the state and observation equations. That is,*

$$\begin{aligned} \mathbf{Z}_{t_k} &= \Phi(\mathbf{Z}_{t_{k-1}}, t_{k-1}; t_k) + \mathbf{W}_{t_k}, & \mathbf{W}_{t_k} &\sim \mathcal{N}_d(0, Q_k), \\ \mathbf{Y}_{t_k} &= C\mathbf{Z}_{t_k} + \mathbf{V}_{t_k}, & \mathbf{V}_{t_k} &\sim \mathcal{N}_{d_y}^k(0, R_k), \end{aligned} \quad (3.6)$$

where $C \in \mathbb{R}^{d_y \times d}$. In this case, the transition density for a given ancestor $j \in \{1, \dots, N_f\}$ is $f_k(\mathbf{z}_{t_{k-1}}^{(j)}, \mathbf{z}_{t_k}) = \mathcal{N}_d(\mathbf{z}_{t_k}; \boldsymbol{\mu}_k^{(j)}, Q_k)$, where $\boldsymbol{\mu}_k^{(j)} := \Phi(\mathbf{z}_{t_{k-1}}^{(j)}, t_{k-1}; t_k)$, and the likelihood is $g_k(\mathbf{z}_{t_k}, \mathbf{y}_{t_k}) = \mathcal{N}_{d_y}^k(\mathbf{y}_{t_k}; C\mathbf{z}_{t_k}, R_k)$. Since both densities are Gaussian, the product $f_k \cdot g_k$ is proportional to a Gaussian in \mathbf{z}_{t_k} for each fixed j . Completing the square yields the conditional $\pi_k^{N_f}(\mathbf{z}_{t_k} | j) = \mathcal{N}_d(\mathbf{z}_{t_k}; \mathbf{m}_k^{(j)}, \Sigma_k)$, where

$$\begin{aligned} \Sigma_k &= (Q_k^{-1} + C^\top R_k^{-1} C)^{-1}, \\ \mathbf{m}_k^{(j)} &= \Sigma_k (Q_k^{-1} \boldsymbol{\mu}_k^{(j)} + C^\top R_k^{-1} \mathbf{y}_{t_k}). \end{aligned} \quad (3.7)$$

Marginalizing over j with the uniform prior $p(j) = 1/N_f$, the approximate filter distribution is a Gaussian mixture

$$\pi_k^{N_f}(\mathbf{z}_{t_k}) = \frac{1}{N_f} \sum_{j=1}^{N_f} w_k^{(j)} \mathcal{N}_d(\mathbf{z}_{t_k}; \mathbf{m}_k^{(j)}, \Sigma_k), \quad (3.8)$$

where the mixture weights $w_k^{(j)} \propto \mathcal{N}_{d_y}^k(\mathbf{y}_{t_k}; C\boldsymbol{\mu}_k^{(j)}, CQ_kC^\top + R_k)$ are the marginal likelihoods of each component. Sampling N_a samples from this distribution is straightforward: first draw j from the categorical distribution with probabilities proportional to $\{w_k^{(j)}\}_{j=1}^{N_f}$, then draw $\mathbf{z}_{t_k} \sim \mathcal{N}_d(\mathbf{m}_k^{(j)}, \Sigma_k)$. In other words, we are sampling from the filter approximation in (3.4) instead of (3.5).

Consequently, when the observation model is linear-Gaussian, no MCMC iterations are needed; one can draw independent and exact samples from $\pi_k^{N_f}$ at each assimilation step, which eliminates burn-in and correlation between successive samples. The covariance Σ_k and its Cholesky factor can be precomputed once since they do not depend on j .

Example 3.2 (Non-Gaussian likelihood – MCMC sampling). When the observation operator \mathcal{O}_{t_k} is nonlinear-Gaussian, or when it is linear but the observation noise is non-Gaussian, the product $f_k \cdot g_k$ is no longer Gaussian in \mathbf{z}_{t_k} . Consequently, the closed-form mixture representation in [Example 3.1](#) is no longer available (unless one adopts specific parameterizations based on transport maps; see [\[15\]](#)). In particular, even when \mathcal{O}_{t_k} is linear, a non-Gaussian error distribution prevents the likelihood from combining with the Gaussian transition densities into a single tractable distribution, thereby precluding direct sampling. In either setting, one must instead resort to MCMC sampling from the joint distribution $\pi_k^{N_f}(\mathbf{z}_{t_k}, j)$ in [\(3.5\)](#).

Our implementation supports four MCMC kernels: Random Walk Metropolis with Gibbs (RWM-Gibbs), Preconditioned Crank–Nicolson (pCN) [\[10\]](#), Metropolis-Adjusted Langevin Algorithm (MALA) [\[47\]](#), and Hamiltonian Monte Carlo (HMC) [\[42\]](#). In all four kernels, the auxiliary variable j can be updated jointly or via a separate Gibbs step, and step-size parameters are adaptively tuned during a burn-in phase to achieve a target acceptance rate; see [\[51\]](#) for a related discussion.

Cost of SMCMC Algorithm

The SMCMC method proved particularly effective and efficient in high-dimensional problems. Since both Q_k and R_k are diagonal (see [Section 2](#)), evaluating f_k and g_k requires only element-wise operations over d and d_y^k components, respectively. Therefore, the cost of each MCMC step is $\mathcal{O}(d + d_y^k)$, and the total cost of the SMCMC algorithm per assimilation cycle is $\mathcal{O}([d + d_y^k]N_a)$. On a multi-core machine, the element-wise operations are naturally parallelized across cores.

In light of [\(2.1\)–\(2.3\)](#), the SMCMC filtering method of [\[49\]](#) is summarized in [Algorithm A.1](#) in the Appendix.

4 Localized Sequential MCMC Filter

In many practical applications, the observational locations tend to be very sparse or highly localized in space. As an example of such applications is the set of data obtained from the SWOT mission led by NASA. It aims to provide high-resolution, detailed measurements across large swaths of oceans, lakes, and rivers with unprecedented accuracy collected via innovative interferometric radars. This set of data is expected to enhance predictive DA models by providing accurate initial and boundary conditions as well as accurate observations, thus improving forecasts for climate, weather, and hydrological systems. Another example is the set of ocean data collected via the so-called ocean drifters, which are floating devices equipped with sensors that collect vital data on ocean currents, water velocities, and temperatures as they drift with the flow of the water. These drifters are deployed across the globe, but their distribution is often sparse, especially in remote regions like the polar seas or vast stretches of the open ocean.

In these situations, filtering the entire signal \mathbf{Z}_{t_k} all at once would be computationally impractical. Instead, a more attractive approach would be to focus the filtering on the specific regions and time points where observations are available, rather than attempting to filter the entire signal as a whole. The basic idea behind our localization scheme is to perform a domain localization where the domain \mathbf{G} is partitioned into Γ subdomains $\mathbf{G} = \bigcup_{i=1}^{\Gamma} G_i$, and then, to find all subdomains G_i 's that contain observational locations and update the state variables in these subdomains. Note that this partition can be time-dependent; in other words, one can increase or decrease the number of subdomains Γ at time t to adopt the distribution of observations coming at this particular time. Let $\bar{\mathbf{x}}_{t_k} \subset \mathbf{G}$ denote the collection of grid points inside the subdomains that contain observational locations at time t_k . Let $\mathbf{z}_{t_k}(\bar{\mathbf{x}}_{t_k}) \in \mathbb{R}^{d_k}$, $d_k < d$, be a sub-vector of the whole hidden signal \mathbf{z}_{t_k} with variables at locations $\bar{\mathbf{x}}_{t_k}$.

We present two variants of the localized SMCMC filter, which we illustrate in [Figure 1](#). Both variants share the common idea of restricting the MCMC updates to the observed region, but they differ in how they decompose the problem and blend the resulting updates.

4.1 Variant 1: Joint Observed-Block Localization

The first variant collects all subdomains that contain observations into a single combined observed region and generates posterior samples over this reduced domain. Specifically, at the first observation time t_1 , one draws N_a

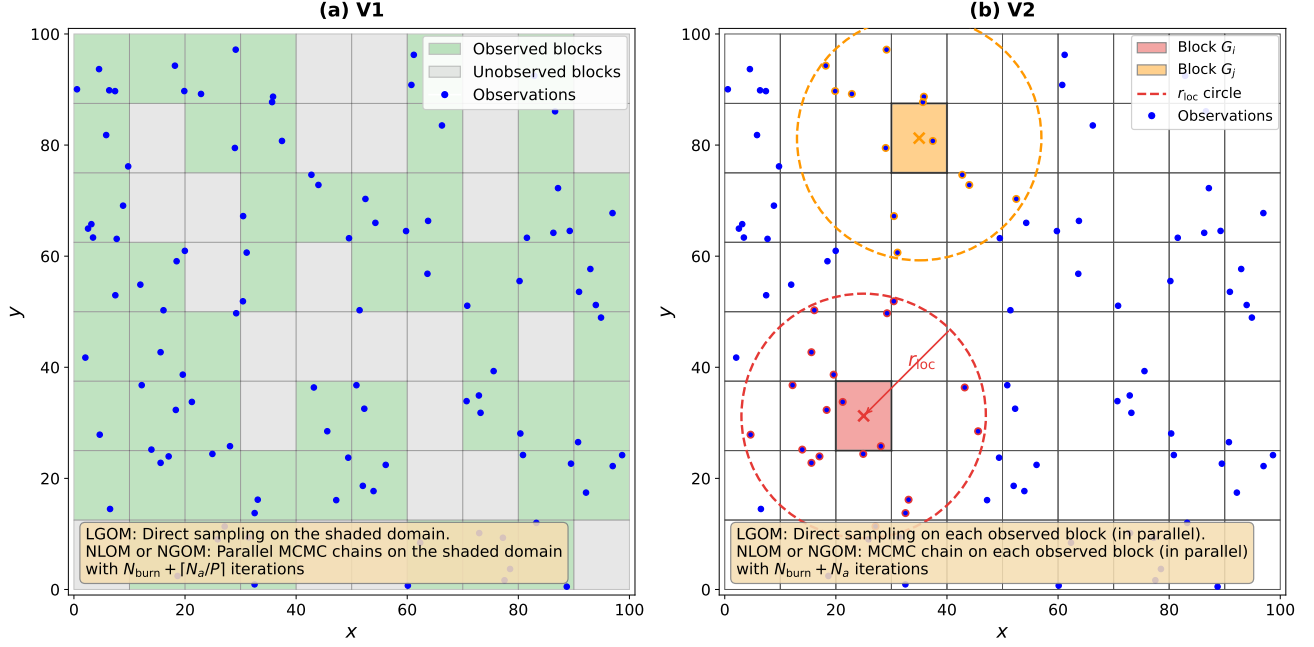


Figure 1: Illustration of the two localization strategies on a 100×100 grid with 80 blocks and randomly placed observations (LGOM = Linear Gaussian Observation Model; NLGOM = Non-Linear Gaussian Observation Model; NGOM = Non-Gaussian Observation Model). (a) V1 joint localization: observed blocks (green) are updated jointly; unobserved blocks (gray) retain their forecast values. For an LGOM the posterior is sampled directly; for an NLGOM or NGOM P parallel MCMC chains of length $N_{\text{burn}} + \lceil N_a/P \rceil$ are run on the combined shaded domain. (b) V2 per-block halo localization: each observed block is updated independently using observations that fall within a halo of radius r_{loc} . For an LGOM the blocks are sampled directly in parallel; for an NLGOM or NGOM each block runs an MCMC chain of length $N_{\text{burn}} + N_a$ in parallel.

samples $\{\mathbf{z}_{t_1}^{(i)}(\bar{\mathbf{x}}_{t_1})\}_{1 \leq i \leq N_a}$ from the distribution

$$\tilde{\pi}_1(\mathbf{z}_{t_1}(\bar{\mathbf{x}}_{t_1})) \propto \tilde{g}_1(\mathbf{z}_{t_1}(\bar{\mathbf{x}}_{t_1}), \mathbf{y}_{t_1}) \tilde{f}_1(\mathbf{z}_0(\bar{\mathbf{x}}_{t_1}), \mathbf{z}_{t_1}(\bar{\mathbf{x}}_{t_1})). \quad (4.1)$$

At subsequent times t_k , $k > 1$, the localized filtering distribution is

$$\tilde{\pi}_k^{N_f}(\mathbf{z}_{t_k}(\bar{\mathbf{x}}_{t_k})) \propto \tilde{g}_k(\mathbf{z}_{t_k}(\bar{\mathbf{x}}_{t_k}), \mathbf{y}_{t_k}) \frac{1}{N_f} \sum_{j=1}^{N_f} \tilde{f}_k(\mathbf{z}_{t_{k-1}}^{(j)}(\bar{\mathbf{x}}_{t_k}), \mathbf{z}_{t_k}(\bar{\mathbf{x}}_{t_k})). \quad (4.2)$$

When the observation model is linear-Gaussian, (4.2) is a Gaussian mixture from which N_a independent samples can be drawn directly (Example 3.1). Otherwise, one introduces the ancestor index j and draws N_a samples $\{\mathbf{z}_{t_k}^{(i)}(\bar{\mathbf{x}}_{t_k}), j_i\}_{1 \leq i \leq N_a}$ from the joint distribution

$$\tilde{\pi}_k^{N_f}(\mathbf{z}_{t_k}(\bar{\mathbf{x}}_{t_k}), j) \propto \tilde{g}_k(\mathbf{z}_{t_k}(\bar{\mathbf{x}}_{t_k}), \mathbf{y}_{t_k}) \tilde{f}_k(\mathbf{z}_{t_{k-1}}^{(j)}(\bar{\mathbf{x}}_{t_k}), \mathbf{z}_{t_k}(\bar{\mathbf{x}}_{t_k})) p(j), \quad (4.3)$$

using an appropriate MCMC kernel (Example 3.2). The density \tilde{f}_k can be thought of as the restriction of the transition density f_k on subdomains G_i 's with locations $\bar{\mathbf{x}}_{t_k}$, and \tilde{g}_k is the likelihood density resulting from a modified observational model $\tilde{\mathcal{O}}_{t_k} : \mathbb{R}^{d_k} \rightarrow \mathbb{R}^{d_y}$. For instance, if $\mathcal{O}_{t_k} = C\mathbf{z}_{t_k}$ for some matrix $C \in \mathbb{R}^{d_y \times d}$, then one would modify C by keeping only the columns that correspond to $\mathbf{z}_{t_k}(\bar{\mathbf{x}}_{t_k})$ and have $\tilde{\mathcal{O}}_{t_k} = \tilde{C}\mathbf{z}_{t_k}(\bar{\mathbf{x}}_{t_k})$, where $\tilde{C} \in \mathbb{R}^{d_y \times d_k}$ is the new modified matrix. After obtaining the samples $\mathbf{z}_{t_k}(\bar{\mathbf{x}}_{t_k})$, one updates the rest of the variables (that is, update $\mathbf{z}_{t_k}(\bar{\mathbf{x}}_{t_k}^c)$, where $\bar{\mathbf{x}}_{t_k}^c$ refers to the complement $G \setminus \bar{\mathbf{x}}_{t_k}$) according to the dynamics in the forward model. In light of (2.1)–(2.3), for a given $j \in \{1, \dots, N_f\}$, one would have

$$\tilde{f}_k(\mathbf{z}_{t_{k-1}}^{(j)}(\bar{\mathbf{x}}_{t_k}), \mathbf{z}_{t_k}(\bar{\mathbf{x}}_{t_k})) \propto \exp \left\{ -\frac{1}{2} [\mathbf{z}_{t_k}(\bar{\mathbf{x}}_{t_k}) - \bar{\boldsymbol{\mu}}_k^{(j)}]^\top \widetilde{Q}_k^{-1} [\mathbf{z}_{t_k}(\bar{\mathbf{x}}_{t_k}) - \bar{\boldsymbol{\mu}}_k^{(j)}] \right\}, \quad (4.4)$$

where $\bar{\boldsymbol{\mu}}_k^{(j)} := \Phi(\mathbf{Z}_{t_{k-1}}^{(j)}, t_{k-1}; t_k)(\bar{\mathbf{x}}_{t_k})$ and \widetilde{Q}_k^{-1} is the matrix with rows and columns of Q_k^{-1} that correspond to the grid subdomains that contain the locations $\bar{\mathbf{x}}_{t_k}$. The steps of this variant are summarized in [Algorithm 1](#). We note that the localization described here is not limited to SSMs with Gaussian noise, but it can be applied to any SSM as long as the noise covariance matrix Q_k and its inverse can be computed or estimated.

Algorithm 1 : LSMCMC – Variant 1 (Joint Observed-Block Localization)

Input: Matrices Q_k, Q_k^{-1} ; partition $\mathbf{G} = \bigcup_{i=1}^{\Gamma} G_i$; initial state $\check{\mathbf{Z}}_0 = \mathbf{z}_0$; observations $\{\mathbf{y}_{t_k}\}_{k \geq 1}$ and their locations; number of forecast samples N_f ; number of analysis samples $N_a \geq N_f$; time-lag L . Set $\tau_k := (t_k - t_{k-1})/L$.

1. **Initialize** ($k = 1$):

- (a) Forecast: for $l = 0, \dots, L - 1$, compute $\check{\mathbf{Z}}_{(l+1)\tau_1} = \Phi(\check{\mathbf{Z}}_{l\tau_1}, l\tau_1; (l+1)\tau_1)$.
- (b) Identify the subdomains containing observations at t_1 ; collect $\bar{\mathbf{x}}_{t_1}$ and extract sub-matrix \widetilde{Q}_1^{-1} .
- (c) Add noise: $\check{\mathbf{Z}}_{t_1} := \check{\mathbf{Z}}_{t_1} + \mathbf{W}_{t_1}$, $\mathbf{W}_{t_1} \sim \mathcal{N}_d(0, Q_1)$.
- (d) Generate N_a samples $\{\mathbf{Z}_{t_1}^{(i)}(\bar{\mathbf{x}}_{t_1})\}_{i=1}^{N_a}$ from (4.1)—either by direct sampling when the SSM is as in [Example 3.1](#), or by running an MCMC kernel initialized at $\check{\mathbf{Z}}_{t_1}(\bar{\mathbf{x}}_{t_1})$ otherwise ([Example 3.2](#)). The unobserved components $\bar{\mathbf{x}}_{t_1}^c$ retain the forecast value $\check{\mathbf{Z}}_{t_1}(\bar{\mathbf{x}}_{t_1}^c)$.
- (e) Estimate the filter mean $\widehat{\mathbf{m}}_{t_1}: \widehat{\mathbf{m}}_{t_1}(\bar{\mathbf{x}}_{t_1}) \leftarrow \frac{1}{N_a} \sum_{i=1}^{N_a} \mathbf{Z}_{t_1}^{(i)}(\bar{\mathbf{x}}_{t_1})$ and $\widehat{\mathbf{m}}_{t_1}(\bar{\mathbf{x}}_{t_1}^c) \leftarrow \check{\mathbf{Z}}_{t_1}(\bar{\mathbf{x}}_{t_1}^c)$.
- (f) Reduce the N_a samples to N_f analysis members (e.g. by random grouping and averaging) and update only the observed cells $\bar{\mathbf{x}}_{t_1}$ for the next forecast step.

2. **For** $k = 2, \dots, T$:

- (a) Forecast: for each $i = 1, \dots, N_f$, propagate $\check{\mathbf{Z}}_{(l+1)\tau_k + t_{k-1}}^{(i)} = \Phi(\check{\mathbf{Z}}_{l\tau_k + t_{k-1}}^{(i)}, l\tau_k + t_{k-1}; (l+1)\tau_k + t_{k-1})$ for $l = 0, \dots, L - 1$, with $\check{\mathbf{Z}}_{t_{k-1}}^{(i)} = \mathbf{Z}_{t_{k-1}}^{(i)}$.
- (b) Identify subdomains with observations at t_k ; collect $\bar{\mathbf{x}}_{t_k}$ and extract sub-matrix \widetilde{Q}_k^{-1} .
- (c) Add noise: $\check{\mathbf{Z}}_{t_k}^{(i)} := \check{\mathbf{Z}}_{t_k}^{(i)} + \mathbf{W}_{t_k}^{(i)}$, $\mathbf{W}_{t_k}^{(i)} \sim \mathcal{N}_d(0, Q_k)$, for $i = 1, \dots, N_f$.
- (d) Generate N_a samples $\{\mathbf{Z}_{t_k}^{(i)}(\bar{\mathbf{x}}_{t_k})\}_{i=1}^{N_a}$ from $\tilde{\pi}_k^{N_f}$ in (4.2)—either by direct sampling when the SSM is as in [Example 3.1](#) or by running an MCMC kernel otherwise ([Example 3.2](#)). The unobserved components $\bar{\mathbf{x}}_{t_k}^c$ are not sampled; each forecast member retains its forecast state at those locations.
- (e) Estimate the filter mean $\widehat{\mathbf{m}}_{t_k}: \widehat{\mathbf{m}}_{t_k}(\bar{\mathbf{x}}_{t_k}) \leftarrow \frac{1}{N_a} \sum_{i=1}^{N_a} \mathbf{Z}_{t_k}^{(i)}(\bar{\mathbf{x}}_{t_k})$ and $\widehat{\mathbf{m}}_{t_k}(\bar{\mathbf{x}}_{t_k}^c) \leftarrow \frac{1}{N_f} \sum_{i=1}^{N_f} \check{\mathbf{Z}}_{t_k}^{(i)}(\bar{\mathbf{x}}_{t_k}^c)$.
- (f) Reduce the N_a samples to N_f analysis members (e.g. by random grouping and averaging) and update only the observed cells $\bar{\mathbf{x}}_{t_k}$ of the ensemble for the next forecast step.

Output: Return $\{\widehat{\mathbf{m}}_{t_k}\}_{k \in \{1, \dots, T\}}$.

4.2 Variant 2: Halo-Based Per-Block Localization

While the joint approach of Variant 1 reduces the state dimension from d to d_k , the effective dimension can still be large when many subdomains contain observations. Variant 2, which we call *halo-based per-block localization*, processes each observed subdomain independently, thereby decomposing the problem into many smaller, fully parallel MCMC chains.

For each observed subdomain G_i , we define an extended neighborhood (or *halo*) $\widehat{G}_i \supseteq G_i$ that includes all grid points within a prescribed radius r_h (measured in grid points) of the centroid \mathbf{c}_i of G_i . The halo provides spatial context: the local likelihood is evaluated using all observations whose locations fall within \widehat{G}_i , with observation noise inflated via Gaspari–Cohn tapering so that distant observations have progressively less influence. Let $\widehat{\mathbf{x}}_{t_k}^{(i)}$

and $\mathbf{y}_{t_k}^{(i)}$ denote the grid points and local observations in \widehat{G}_i , respectively. The local target distribution for block i is defined over the halo state:

$$\widehat{\pi}_k^{(i)}(\mathbf{z}_{t_k}(\widehat{\mathbf{x}}_{t_k}^{(i)}), j) \propto \widehat{g}_k^{(i)}(\mathbf{z}_{t_k}(\widehat{\mathbf{x}}_{t_k}^{(i)}), \mathbf{y}_{t_k}^{(i)}) \widehat{f}_k^{(i)}(\mathbf{Z}_{t_{k-1}}(\widehat{\mathbf{x}}_{t_k}^{(i)}), \mathbf{z}_{t_k}(\widehat{\mathbf{x}}_{t_k}^{(i)})) p(j), \quad (4.5)$$

where $\widehat{f}_k^{(i)}$ is the restriction of the transition density to the halo and $\widehat{g}_k^{(i)}$ is the corresponding local likelihood evaluated with GC-tapered observation noise (4.6).

To smoothly downweight the influence of distant observations without introducing discontinuities, we taper the observation-error variance using the Gaspari–Cohn function $S(\cdot)$ [26]. For each local observation j at location $\mathbf{x}_j \in \widehat{G}_i$, the effective observation noise standard deviation is inflated as

$$\tilde{\sigma}_{y,j}^{(i)} = \frac{\sigma_{y,j}}{\sqrt{S\left(\frac{\|\mathbf{x}_j - \mathbf{c}_i\|}{r_h}\right)}}, \quad (4.6)$$

where \mathbf{c}_i is the centroid of G_i . The Gaspari–Cohn function S is compactly supported with $S(0) = 1$ and $S(r) = 0$ for $r \geq 2$, and is defined by

$$S(r) = \begin{cases} 1 - \frac{5}{3}r^2 + \frac{5}{8}r^3 + \frac{1}{2}r^4 - \frac{1}{4}r^5, & 0 \leq r \leq 1, \\ 4 - 5r + \frac{5}{3}r^2 + \frac{5}{8}r^3 - \frac{1}{2}r^4 + \frac{1}{12}r^5 - \frac{2}{3r}, & 1 < r \leq 2, \\ 0, & r > 2. \end{cases} \quad (4.7)$$

Observations at the block center retain their nominal precision, while observations near the halo boundary have greatly inflated noise and thus negligible influence. This tapering avoids sharp boundaries in the analysis without requiring any post-hoc blending of overlapping updates.

After sampling, only the state variables at the block cells G_i are retained. For an LGOM, the diagonal prior allows the non-block halo variables to be integrated out analytically, so that N_a samples are drawn directly in dimension $|G_i|$. For an NLGOM or NGOM, the MCMC chain operates on the full halo state in dimension $|\widehat{G}_i|$, and only the block-cell components are kept from the resulting samples. Because the partition $\{G_i\}$ is non-overlapping, each grid point is updated by at most one block, and grid points that do not belong to any observed block retain their forecast values.

The key advantage of the per-block halo scheme is that the problems for distinct blocks i are independent and can be solved in parallel. Each block’s effective sampling dimension is $|G_i|$ for an LGOM or $|\widehat{G}_i|$ for an NLGOM or NGOM, both much smaller than d , and the halo provides spatial context through its local observations at essentially no extra cost because the prior covariance is diagonal. In our implementation, we use a thread pool to parallelize over all observed blocks simultaneously. The total cost per assimilation step is then $\mathcal{O}([\kappa(|\widehat{G}_i|) + \kappa_y(\widehat{d}_{y,\max})]N_a/P)$, where $\widehat{d}_{y,\max} = \max_i |\mathbf{y}_{t_k}^{(i)}|$ and P is the number of parallel threads. The halo radius r_h controls the trade-off between accuracy (larger halos capture more distant observations) and efficiency (smaller halos yield fewer local observations and a smaller MCMC state for an NLGOM or NGOM). The steps of this variant are summarized in Algorithm 2.

Algorithm 2 : LSMCMC – Variant 2 (Halo-Based Per-Block Localization)

Input: Matrices Q_k, Q_k^{-1} ; partition $\mathbf{G} = \bigcup_{i=1}^{\Gamma} G_i$; halo radius r_h ; initial state $\check{\mathbf{Z}}_0 = \mathbf{z}_0$; observations $\{\mathbf{y}_{t_k}\}_{k \geq 1}$ and their locations; number of forecast samples N_f ; number of analysis samples $N_a \geq N_f$; time-lag L . Set $\tau_k := (t_k - t_{k-1})/L$.

1. **Initialize** ($k = 1$):

- (a) Forecast: for $l = 0, \dots, L - 1$, compute $\check{\mathbf{Z}}_{(l+1)\tau_1} = \Phi(\check{\mathbf{Z}}_{l\tau_1}, l\tau_1; (l+1)\tau_1)$.
- (b) Add noise: $\check{\mathbf{Z}}_{t_1} := \check{\mathbf{Z}}_{t_1} + \mathbf{W}_{t_1}$, $\mathbf{W}_{t_1} \sim \mathcal{N}_d(0, Q_1)$.
- (c) Identify all observed subdomains $\{G_i : \widehat{G}_i \cap \text{obs. locations} \neq \emptyset\}$. For each such G_i , construct halo \widehat{G}_i , extract local observations $\mathbf{y}_{t_1}^{(i)}$, and compute GC-tapered observation noise via (4.6).

- (d) **In parallel** over observed blocks i : draw N_a samples from $\hat{\pi}_1^{(i)}$ in (4.5) (direct sampling in dimension $|G_i|$ for LGOM; MCMC in dimension $|\widehat{G}_i|$ for NLGOM or NGOM), using halo observations with GC-tapered noise; retain only block cells G_i . Compute the local posterior mean $\bar{\mathbf{z}}_{t_1}^{(i)}(G_i)$.
- (e) For each observed block i , reduce the N_a local samples to N_f analysis members (e.g. by random grouping and averaging) and overwrite only the block cells G_i of the N_f forecast members. Grid points outside all observed blocks retain their forecast values.

2. **For** $k = 2, \dots, T$:

- (a) Forecast: for each $i = 1, \dots, N_f$, propagate $\check{\mathbf{Z}}_{(l+1)\tau_k+t_{k-1}}^{(i)} = \Phi(\check{\mathbf{Z}}_{l\tau_k+t_{k-1}}^{(i)}, l\tau_k + t_{k-1}; (l+1)\tau_k + t_{k-1})$ for $l = 0, \dots, L-1$, with $\check{\mathbf{Z}}_{t_{k-1}}^{(i)} = \mathbf{Z}_{t_{k-1}}^{(i)}$.
- (b) Add noise: $\tilde{\mathbf{Z}}_{t_k}^{(i)} := \check{\mathbf{Z}}_{t_k}^{(i)} + \mathbf{W}_{t_k}^{(i)}$, $\mathbf{W}_{t_k}^{(i)} \sim \mathcal{N}_d(0, Q_k)$, for $i = 1, \dots, N_f$.
- (c) Identify observed subdomains at t_k . For each, construct halo \widehat{G}_i , extract local observations $\mathbf{y}_{t_k}^{(i)}$, and compute GC-tapered observation noise via (4.6).
- (d) **In parallel** over observed blocks i : draw N_a samples from $\hat{\pi}_k^{(i)}$ in (4.5) (direct for LGOM in $|G_i|$; MCMC for NLGOM or NGOM in $|\widehat{G}_i|$), using halo observations with GC-tapered noise; retain only block cells G_i . Compute the local posterior mean $\bar{\mathbf{z}}_{t_k}^{(i)}(G_i)$.
- (e) For each observed block i , reduce the N_a local samples to N_f analysis members (e.g. by random grouping and averaging) and overwrite only the block cells G_i of the N_f forecast members. Grid points outside all observed blocks retain their forecast values.

Output: Return $\{\hat{\pi}_k^{N_a}(\varphi)\}_{k \in \{1, \dots, T\}}$.

Remark 4.1. When additional computing resources are available, one may run $M > 1$ independent LSMCMC (V1 or V2) experiments in parallel and average their posterior estimates to reduce Monte Carlo variance: $\hat{\pi}_k^{N_a}(\varphi) \leftarrow \frac{1}{M} \sum_{m=1}^M \hat{\pi}_k^{(m)}(\varphi)$, where $\hat{\pi}_k^{(m)}$ denotes the estimate from run m .

Remark 4.2. In many applications, the covariance matrix is often time-independent, and therefore, its inverse or the inverse of its Cholesky factor is computed only once at the beginning. In this case, we drop the subscript k in Q_k and Q_k^{-1} in the above algorithms.

5 Numerical Simulations

We demonstrate the proposed LSMCMC schemes on four challenging state-space models: (i) a linear Gaussian model on a 120×120 grid ($d = 14,400$) with SWOT-like observations, (ii) the nonlinear multilayer shallow-water equations (MLSWE) on a 70×80 grid ($d = 67,200$) with a linear-Gaussian observation operator, (iii) the MLSWE with a nonlinear (arctan) observation operator and Gaussian observation noise, and (iv) the MLSWE with the same nonlinear observation operator but non-Gaussian (Cauchy / Student- t , $\nu=1$) observation noise. In each case we compare LSMCMC Variants 1 and 2 against the LETKF [33] with ensemble size K , which is used operationally at several numerical weather prediction centers [50, 25]. All experiments were run on a Linux workstation with 52 CPU cores. LETKF is run in parallel for fair comparison.

5.1 Linear Gaussian Model

5.1.1 Problem setup

Consider the state-space model $\mathbf{Z}_{t_k} = a\mathbf{Z}_{t_{k-1}} + \sigma_z \mathbf{W}_{t_k}$, $\mathbf{Y}_{t_k} = C_k \mathbf{Z}_{t_k} + \sigma_y \mathbf{V}_{t_k}$, where $\mathbf{Z}_{t_k} \in \mathbb{R}^d$ with $d = 120 \times 120 = 14,400$, $a = 0.25$, $\sigma_z = 0.05$, $\sigma_y = 0.05$, and $Q = \sigma_z^2 I_d$, $R_k = \sigma_y^2 I_{d_y}^k$. The observation matrix $C_k \in \mathbb{R}^{d_y^k \times d}$ selects grid points along diagonal SWOT-like swaths that sweep periodically across the domain, simulating the observation pattern of the SWOT satellite altimeter (see Figure 2a). At each cycle, approximately 10–15% of grid points are observed. Because both the state and observation models are linear-Gaussian, the exact Kalman filter (KF) posterior is available analytically, providing a ground-truth benchmark. We run $T = 100$ assimilation cycles.

5.1.2 Parameter choices

We partition the grid into $\Gamma = 900$ blocks for V1 and $\Gamma = 2,400$ blocks for V2. These choices are tuned to get the best RMSE and CPU times. In the linear-Gaussian case, the filtering density is a Gaussian mixture (Example 3.1), so LSMCMC draws N_a independent samples from the exact posterior without MCMC iterations. Table 1 summarizes the key parameters.

Table 1: Parameters for the linear Gaussian experiment.

State dimension $d = 14,400$		Assimilation cycles $T = 100$	
Parameter	LSMCMC V1	LSMCMC V2	LETKF
Blocks Γ	900	2,400	—
Halo / loc. radius	—	$r_h = 1.0$	$h_{loc} = 1.0$
N_f/N_a	50/500	50/500	$K = 50$
RTPP / RTPS	— / —	— / 0.02	1.02 / —

5.1.3 Results

Figure 3 shows the RMSE of each method against the exact KF posterior mean. In the linear Gaussian setting, the KF posterior mean is the minimum-variance estimator, so this RMSE directly measures how close each approximate filter is to the optimal Bayesian solution (it is the most meaningful accuracy metric in this paper). With a single run ($M=1$; see Remark 4.1), V2 already achieves an RMSE of 0.0071, outperforming V1 (0.0203) and very close to LETKF (0.0072), thanks to finer partitioning ($\Gamma=2,400$) and halo localization. Averaging $M=4$ independent runs further reduces the error: V2 reaches **0.0042** at 15 seconds and V1 improves to 0.0101 at 4.5 seconds. Table 2 reports the RMSE and total wall-clock time.

Table 2: Linear Gaussian: RMSE vs KF and wall-clock time. For $M=4$, the reported time is the total time for all four runs which are independent and embarrassingly parallel.

Method	RMSE vs KF	Total Time (s)
LETKF ($K=50$)	0.0072	13
LSMCMC V1 ($M=1$)	0.0203	4
LSMCMC V2 ($M=1$)	0.0071	13
LSMCMC V1 ($M=4$)	0.0101	4.5
LSMCMC V2 ($M=4$)	0.0042	15

The LETKF result is obtained after tuning the localization radius and inflation factor over a grid of $12 \times 14 = 168$ configurations (Figure 2b); small localization radii ($h_{loc} \leq 3$) and mild inflation ($\alpha \approx 1.0$) perform best, with RMSE degrading rapidly as the localization radius grows. Figure 4 compares the filter estimates at the most-observed grid point, confirming that both V1 and V2 track the exact KF solution closely throughout the experiment. Figure 5 displays the spatial analysis fields at cycles 50 and 100; V2 ($M=4$) produces the closest visual match to the KF reference across the entire domain.

5.2 MLSWE with Linear Observation Model

5.2.1 Problem setup

We consider the 3-layer isopycnal MLSWE model over the North Atlantic ($60^\circ\text{W} - 20^\circ\text{W}$, $10^\circ\text{N} - 45^\circ\text{N}$) on a 70×80 Cartesian grid. The state vector includes 12 fields per grid cell (total SSH, u_k, v_k, T_k for $k = 0, 1, 2$), giving a state dimension $d = 12 \times 5,600 = 67,200$. The model is integrated with an RK4 time stepper at $\Delta t = 75$ s. Boundary conditions are prescribed from HYCOM reanalysis, and the bathymetry is derived from ETOPO1 [2]. Because the isopycnal shallow-water equations do not resolve atmospheric heat exchange, the state transition model includes a Newtonian SST nudging term $-\lambda(T - T_{ref})$ in the surface-layer temperature tendency, where T_{ref} is interpolated from HYCOM reanalysis and the relaxation rate $\lambda \approx 2.8 \times 10^{-4} \text{ s}^{-1}$ (time scale $\tau \approx 1$ h). This prevents the model SST from drifting unrealistically in the absence of full thermodynamic forcing.

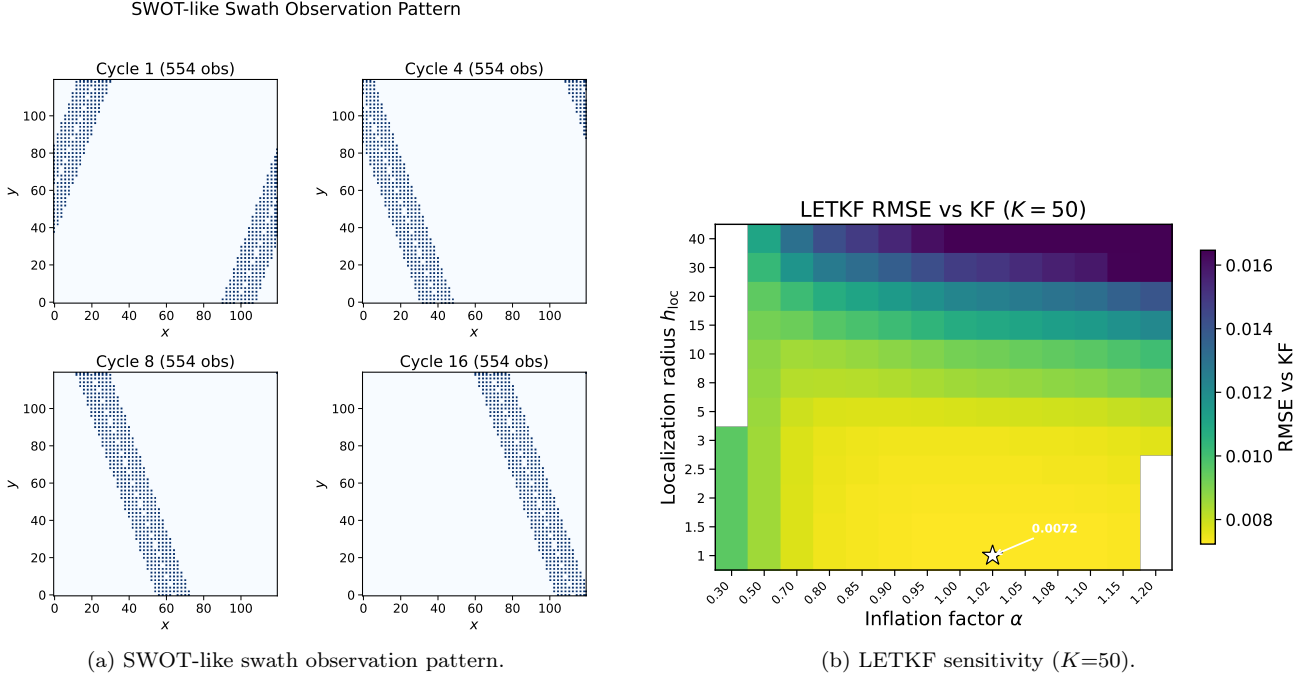


Figure 2: (a) SWOT-like swath observation pattern at selected cycles showing the diagonal sweep across the 120×120 grid. (b) LETKF sensitivity to localization radius h_{loc} and RTPP inflation factor α . The star marks the best configuration ($h_{\text{loc}}=1.0$, $\alpha=1.02$, $\text{RMSE}=0.0072$).

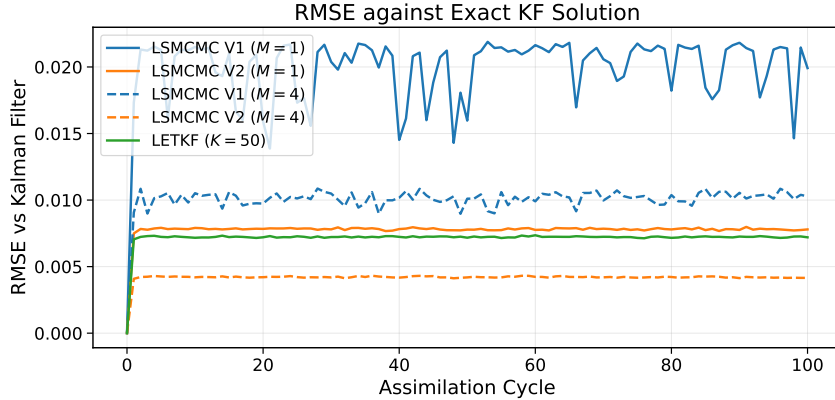


Figure 3: Linear Gaussian experiment ($d=14,400$): RMSE against the exact KF solution over 100 assimilation cycles for LSMCMC V1 and V2 with $M=1$ (solid) and $M=4$ (dashed), and LETKF with $K=50$.

The observation model is linear: $\mathbf{Y}_{t_k} = C_k \mathbf{Z}_{t_k} + \mathbf{V}_{t_k}$, $\mathbf{V}_{t_k} \sim \mathcal{N}(0, R_k)$, where $C_k \in \mathbb{R}^{d_{y_k} \times d}$ extracts velocity, SSH, and SST at observed locations. Observations come from two real-world sources:

1. **Surface drifters** from the NOAA Global Drifter Program (GDP) [37]. Because the GDP hourly product [21] does not yet cover the SWOT science-orbit period (August 2024), we use the quality-controlled 6-hourly interpolated dataset [37] and further interpolate each drifter track to hourly resolution via cubic splines, yielding velocity measurements at ~ 350 – 620 locations per cycle.
2. **SWOT SSH** from the Surface Water and Ocean Topography mission [46, 56], binned onto the model grid with 15% spatial coverage per cycle.

Figure 6 illustrates the spatial coverage of these two observation sources, including the surface drifter positions and SWOT satellite swaths over the model domain.

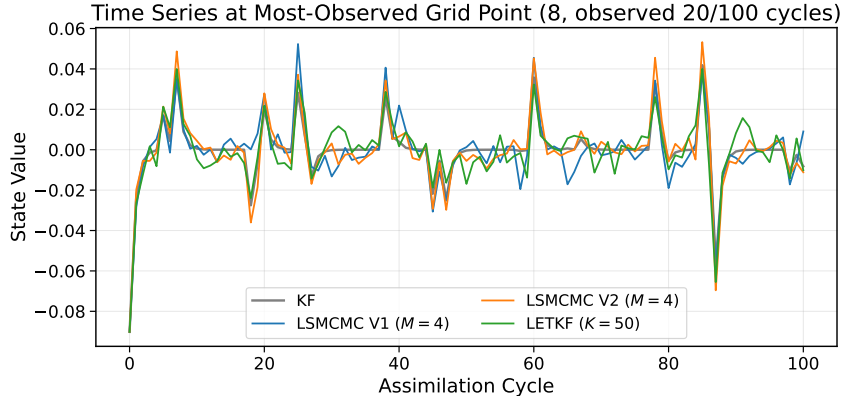


Figure 4: Linear Gaussian: time series at the most-observed grid point comparing LSMCMC V1 and V2 ($M=4$) and LETKF ($K=50$) against the KF.

Observation noise standard deviations are $\sigma_{\text{vel}} = 0.10$ m/s, $\sigma_{\text{SSH}} = 0.25$ m, and $\sigma_{\text{SST}} = 0.40$ K. These values reflect the dominant error sources in each data stream: the GDP velocity error budget is dominated by the cubic-spline interpolation from 6-hourly fixes to hourly resolution (~ 0.05 – 0.10 m/s; [20]); the SWOT SSH noise after spatial averaging onto the 0.5° grid is approximately 0.15 – 0.25 m, accounting for residual mesoscale representation error; and the SST noise of 0.40 K encompasses both instrument error and the sub-grid variability of the SST field.

The forward model noise (process noise) covariance Q is diagonal with standard deviations $\sigma_x^{\text{vel}} = 0.15$ m/s, $\sigma_x^{\text{SSH}} = 0.20$ m, and $\sigma_x^{\text{SST}} = 1.0$ K. Some of these values are chosen to be moderately larger than the observation noise so that the filter assigns sufficient weight to the observations while preventing filter divergence: $\sigma_x^{\text{vel}}/\sigma_{\text{vel}} = 1.5$, and the large $\sigma_x^{\text{SST}} = 1.0$ K compensates for the absence of atmospheric heat fluxes in the isopycnal model, which cannot internally maintain realistic SST without the nudging term. Process noise is applied only to the surface layer; deep layers receive zero process noise because no observations are available at depth and the model dynamics propagate surface corrections downward. We run 240 assimilation cycles (1-hour intervals, 10-day window starting 2024-08-01).

Since the true ocean state is unknown, RMSE is computed at observation locations against the observed values themselves, which serves as a proxy for verification.

5.2.2 Parameter choices

Table 3 summarizes the configuration for all three methods. V1 uses $\Gamma = 50$ blocks and solves a single combined posterior, while V2 uses $\Gamma = 1,400$ fine blocks with halo radius $r_h = 2.5$ grid cells. Both LSMCMC variants use $N_f = 25$ forecast samples and draw $N_a = 500$ analysis samples from the exact Gaussian mixture (Example 3.1). LETKF uses $K = 25$ ensemble members (matching N_f) with localization $h_{\text{loc}} = 60$ km and RTPS relaxation $\alpha = 0.90$.

Table 3: Parameters for the MLSWE linear data model experiment.

State dimension $d = 67,200$		Assimilation cycles $T = 240$	
Parameter	LSMCMC V1	LSMCMC V2	LETKF
Blocks Γ	50	1,400	—
Halo radius r_h	—	2.5	—
$N_f / N_a / K$	25 / 500	25 / 500	— / — / 25
Loc. scale (km)	—	—	60
RTPP / RTPS α	— / —	— / 0.5	0.90 / —
$\sigma_{\text{vel}}, \sigma_{\text{SSH}}, \sigma_{\text{SST}}$		0.10, 0.25, 0.40	
$\sigma_x^{\text{vel}}, \sigma_x^{\text{SSH}}, \sigma_x^{\text{SST}}$		0.15, 0.20, 1.0	

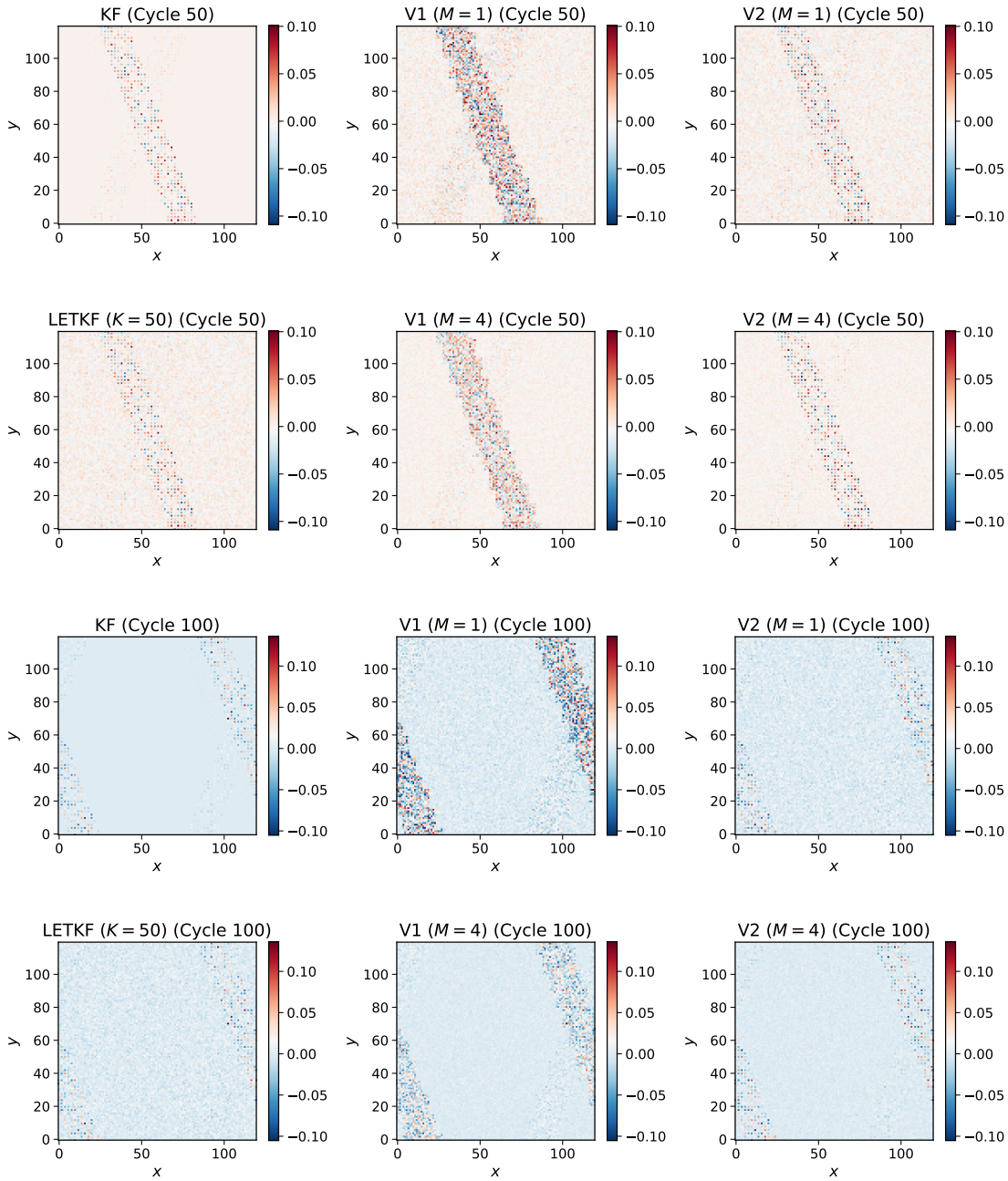


Figure 5: Linear Gaussian: analysis fields at cycle 50 (rows 1–2) and cycle 100 (rows 3–4). Each block shows the KF reference, V1 ($M=1$), and V2 ($M=1$) in the first row, and LETKF ($K=50$), V1 ($M=4$), and V2 ($M=4$) in the second row.

5.2.3 LETKF sensitivity analysis

We perform a sensitivity analysis for LETKF with $K = 25$ and $K = 50$ ensemble members. For each K , we sweep over the localization half-width $h_{\text{loc}} \in \{20, 40, 60, 80, 100, 200, 300\}$ km and RTPP inflation $\alpha \in \{0.5, 0.7, 0.9, 1.0, 1.1\}$. The best configuration for $K = 25$ is $h_{\text{loc}} = 20$ km, $\alpha = 0.9$ (vel RMSE = 0.0078 m/s), and for $K = 50$ it is $h_{\text{loc}} = 60$ km, $\alpha = 0.9$ (vel RMSE = 0.0093 m/s). Notably, small localization radii ($h_{\text{loc}} = 20$ km) perform best for small ensembles, while larger ensembles tolerate wider localization radii. At $h_{\text{loc}} \geq 200$ km, LETKF starts to diverge due to spurious long-range correlations.

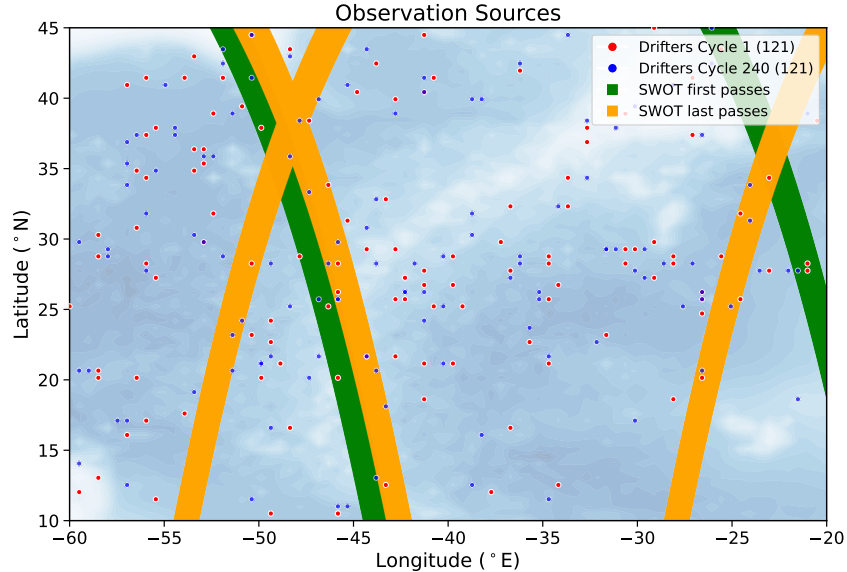


Figure 6: Observation sources: surface drifter positions at cycles 1 and 240 (red and blue dots), and SWOT satellite swaths from first and last passes (green and orange). Bathymetry contours are shown in the background.

5.2.4 Results

Table 4 and Figure 7 show the mean RMSE over 240 cycles for each method. LSMCMC V1 achieves the best velocity RMSE (0.0098 m/s), outperforming LETKF (0.0113 m/s). V2 achieves velocity RMSE of 0.0143 m/s and the best SST RMSE (0.079 K). LETKF leads on SSH (0.362 m vs 0.403 m for V2).

Table 4: MLSWE linear data model: mean RMSE over 240 cycles (vs Observations Values).

Method	Vel RMSE (m/s)	SST RMSE (K)	SSH RMSE (m)	Time/cycle (s)
LETKF ($K=25$)	0.0108	0.111	0.361	1.2
LSMCMC V1 ($\Gamma=50$)	0.0098	0.144	0.493	1.4
LSMCMC V2 ($\Gamma=1400$)	0.0143	0.079	0.403	1.4

All three methods run at approximately 1.2–1.4 s per cycle, making them comparable in wall-clock time. All three methods completed the full 240 cycles without blow-up events. Figure 8 displays the initial and final V1 analysis fields alongside the HYCOM reanalysis. The velocity and SST fields show good qualitative agreement with HYCOM, capturing the large-scale North Atlantic circulation and its mesoscale eddies. The SSH field exhibits noticeable differences, which are expected: the isopycnal MLSWE is a reduced-physics model that does not resolve the full primitive equations, and the presence of islands (e.g., the Azores, Canary Islands) introduces bathymetric effects that the Cartesian solver cannot represent faithfully.

To complement the aggregate RMSE statistics, Figures 9–11 show the analysis time series at the most frequently observed grid cells for each variable. The velocity analysis (Figure 9) tracks the drifter observations closely at both cells, recovering both the mean flow and the higher-frequency fluctuations in eastward and northward velocity. The SST analysis (Figure 10) broadly follows the observed SST evolution, although the match is less tight than for velocity owing to the coarser SST observation density and the SST nudging time scale. For SSH (Figure 11), the observations combine real SWOT altimetric data with synthetic observations drawn from HYCOM on cycles lacking real passes following realistic SWOT swath geometry. Even at the most frequently observed cells the total count remains modest (around 25 over 240 cycles), and neighboring cells often receive far fewer; the analysis tracks a subset of these observations while spreading the altimetric information spatially.

V2’s embarrassingly parallel per-block processing trades slightly higher velocity RMSE for the best SST and SSH performance among all three methods. V2’s architecture across $\Gamma = 1,400$ blocks makes it more scalable to larger grids.

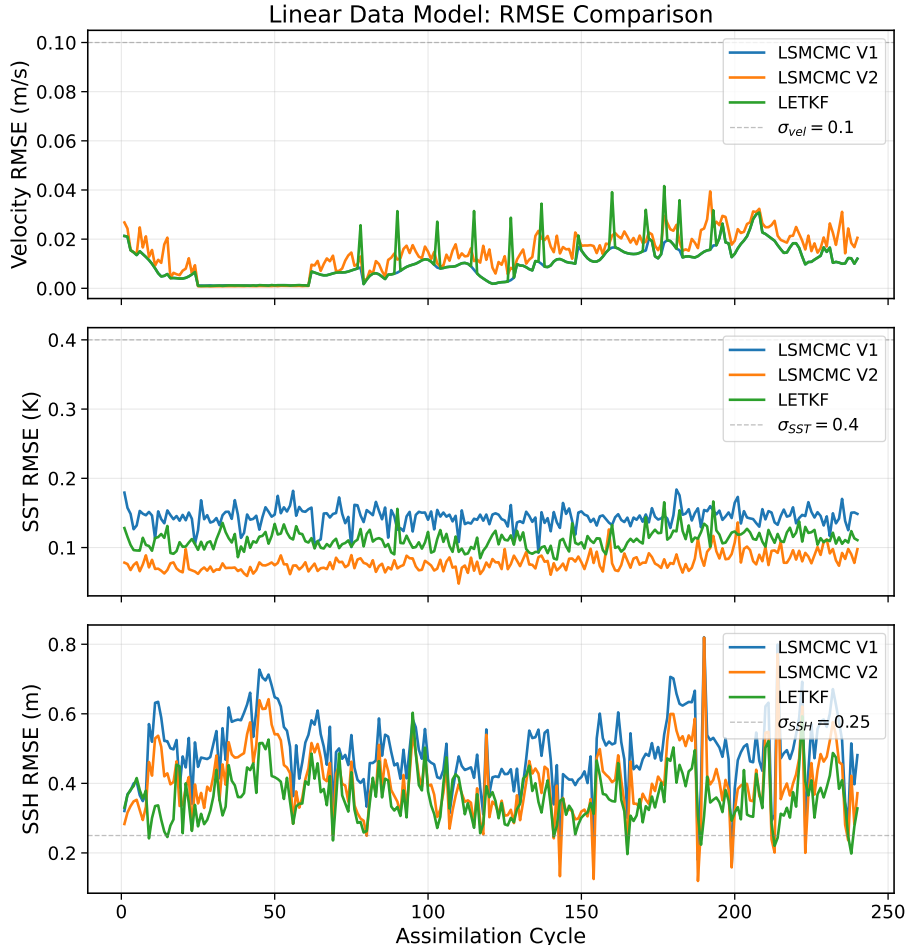


Figure 7: MLSWE with linear observations: velocity, SST, and SSH RMSE comparison of LSMCMC V1, V2, and LETKF ($K=25$) over 240 cycles. Dashed lines indicate observation noise standard deviations.

5.3 MLSWE with Nonlinear Observation Model

5.3.1 Problem setup

We now consider the same MLSWE forward model but with a nonlinear data operator $\mathbf{Y}_{t_k} = \arctan(C_k \mathbf{Z}_{t_k}) + \mathbf{V}_{t_k}$, $\mathbf{V}_{t_k} \sim \mathcal{N}(0, R_k)$. The arctan function compresses the range of the observations and introduces nonlinearity, making the posterior non-Gaussian. In this setting, the exact Gaussian mixture sampling of [Example 3.1](#) is unavailable, and LSMCMC must use an MCMC kernel. We test two kernels for V1: the pCN kernel [\[10\]](#) and HMC kernel [\[42\]](#), where the later exploits gradient information via leapfrog integration. V2 uses the pCN kernel throughout.

Because the arctan function saturates at $\pm\pi/2$, applying it to real observations is physically inconsistent: for example, real sea-surface temperature observations lie in the range $\approx 290\text{--}305\text{ K}$, but $\arctan(300) \approx \pi/2$ regardless of the temperature value, erasing all observational information. The nonlinear observation model is therefore tested exclusively in a synthetic *twin experiment* where observations are generated self-consistently from the arctan operator.

5.3.2 Twin experiment

In the twin experiment, a nature run of the MLSWE model generates the reference trajectory $\{\mathbf{Z}_{t_k}^{\text{nr}}\}$. Synthetic observations are created by $\mathbf{Y}_{t_k} = \arctan(C_k \mathbf{Z}_{t_k}^{\text{nr}}) + \mathbf{V}_{t_k}$. The filter starts from a perturbed initial condition. RMSE is computed over *all grid cells* against the nature run, following standard practice for twin experiments (e.g., [\[40, 29\]](#)). We note that the posterior mean is the conditional expectation given all observations up to time t_k and

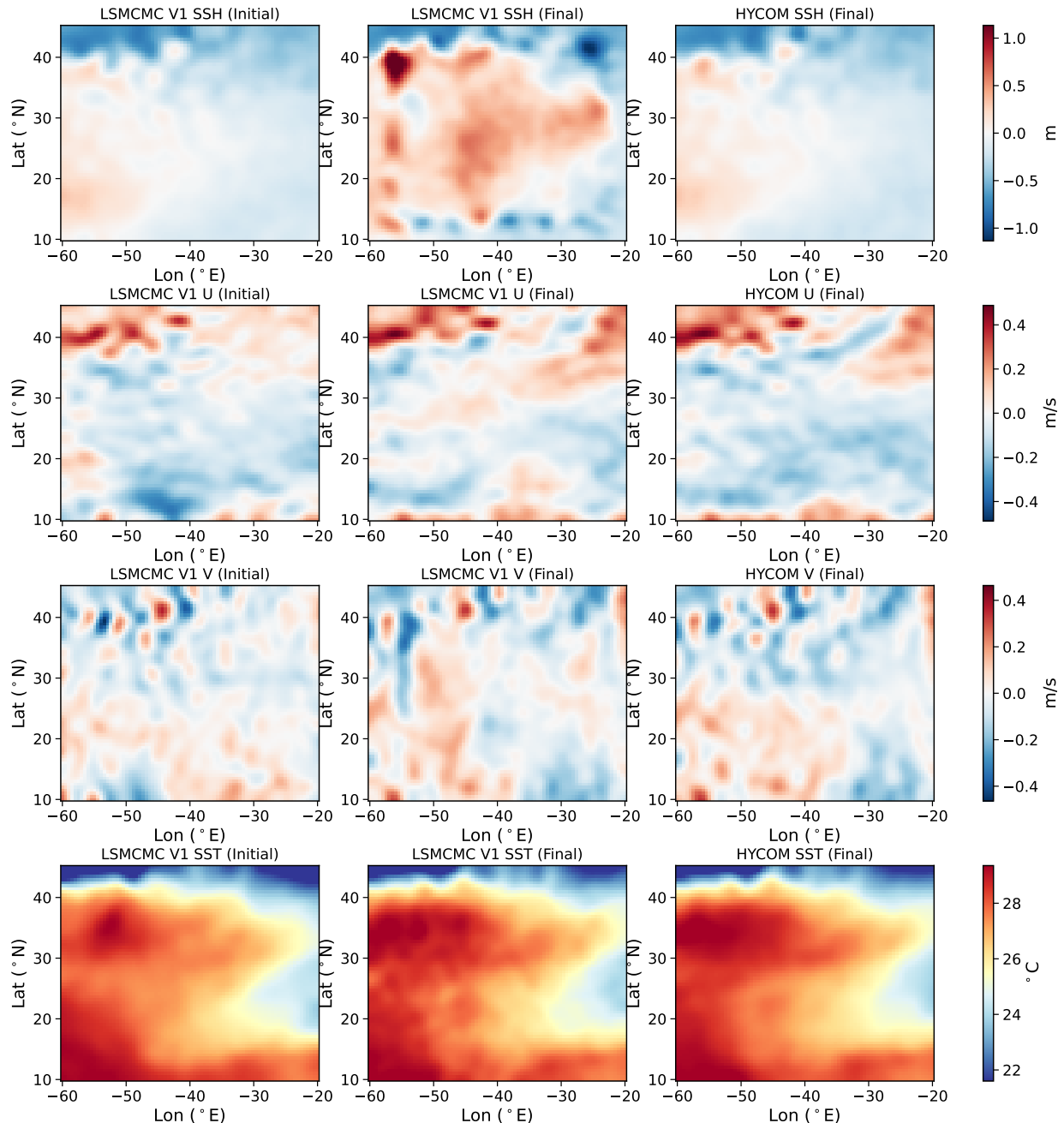


Figure 8: MLSWE linear observation model: initial and final LSMCMC V1 analysis fields (left, centre) and final HYCOM reanalysis (right). Rows show SSH anomaly, eastward velocity u , northward velocity v , and SST. Each row shares a single colour scale; the SSH scale is the average of the analysis and HYCOM ranges.

need not coincide exactly with the nature run, which is a single realization of the stochastic dynamics; lower, non-diverging RMSE nevertheless indicates better filter performance. The forward model noise uses $\sigma_x^{\text{vel}} = 0.15$ m/s, $\sigma_x^{\text{SSH}} = 0.50$ m, and $\sigma_x^{\text{SST}} = 1.0$ K.

Table 5 summarizes the key parameters. The pCN V1 variant uses $N_a = 1,000$ MCMC steps with 500 burn-in and step size $\beta = 0.3$. It runs $P = 10$ chains each chain has a 500 burn-in and $N_a = 100$. The HMC V1 variant uses $N_a = 500$ with 200 burn-in, with $L = 10$ leapfrog steps and initial step size $\varepsilon_0 = 0.5$ (adapted to ~ 0.14). V2 runs per-block pCN chains with $N_a = 2,000$, 500 burn-in, and step size $\beta = 0.81$ (enabled by the smaller per-block dimension).

Table 6 and Figure 12 present the results. The HMC V1 variant outperforms pCN V1 across all three

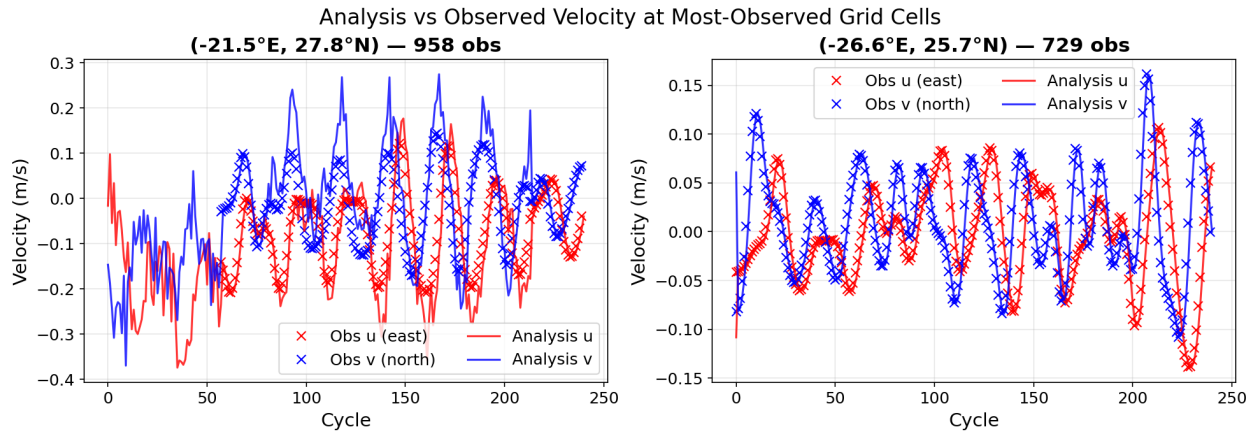


Figure 9: LSMCMC V2 analysis vs. drifter observations: eastward (u) and northward (v) velocity time series at the two most frequently observed grid cells over 240 cycles.

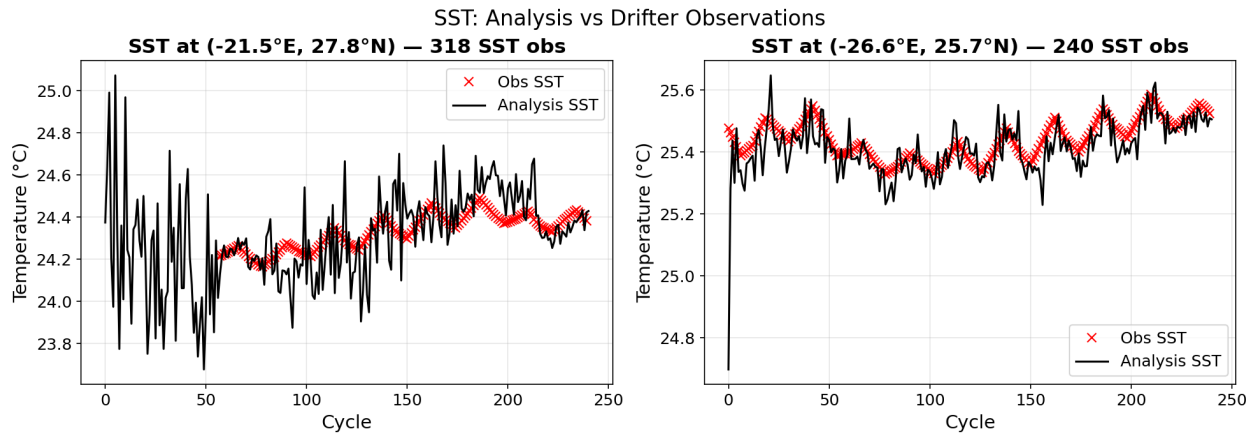


Figure 10: LSMCMC V2 analysis vs. drifter observations: SST time series at the two most frequently observed grid cells.

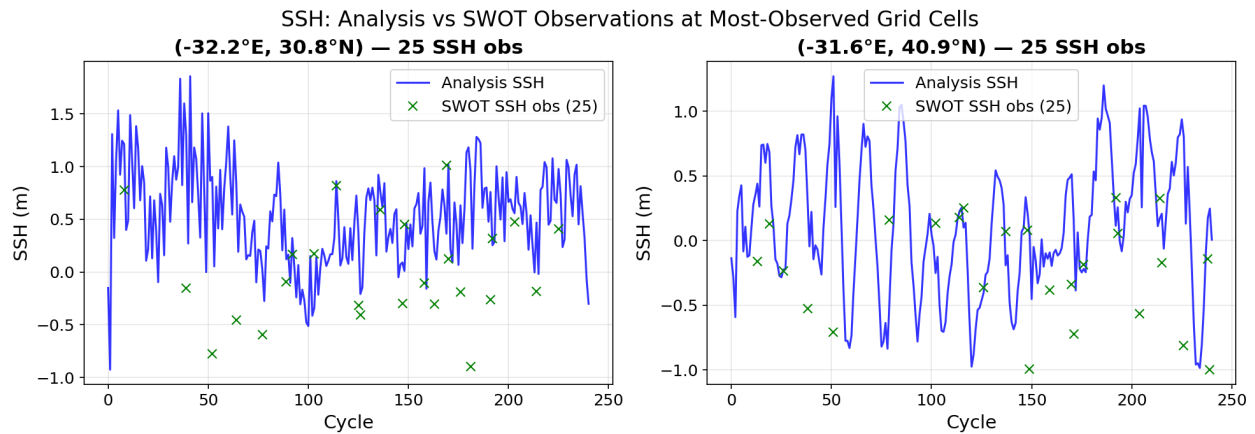


Figure 11: LSMCMC V2 analysis vs. SWOT observations: SSH time series at the two most frequently observed grid cells.

fields (velocity 0.0591 vs 0.0702 m/s, SST 0.389 vs 0.465 K, SSH 0.295 vs 0.346 m), demonstrating that HMC's gradient-guided proposals explore the posterior more effectively in this $\sim 20,000$ -dimensional reduced domain. HMC achieves this with $2\times$ fewer MCMC iterations ($N_a=500$ vs 1,000). V2 outperforms both V1 variants in

Table 5: Parameters for the MLSWE nonlinear twin experiment.

	State dimension $d = 67,200$		Assimilation cycles $T = 240$
Parameter	LSMCMC V1 (pCN)	LSMCMC V1 (HMC)	LSMCMC V2 (pCN)
Blocks Γ	50	50	700
Halo radius r_h	—	—	1.5
N_f / N_a	25 / 1,000	25 / 500	25 / 2,000
Burn-in	500	200	500
MCMC kernel	pCN	HMC	pCN
Step size	$\beta = 0.3$	$\varepsilon_0 = 0.5, L = 10$	$\beta = 0.81$
Adaptive tuning	target 0.40	target 0.65	target 0.35
RTPS α	—	—	0.0
$\sigma_{\text{vel}}, \sigma_{\text{SSH}}, \sigma_{\text{SST}}$		0.10, 0.50, 0.40	
$\sigma_x^{\text{vel}}, \sigma_x^{\text{SSH}}, \sigma_x^{\text{SST}}$		0.15, 0.50, 1.0	

velocity RMSE (0.0546 m/s, a 22% improvement over pCN V1) and SST RMSE (0.362 K), while V1 HMC achieves the best SSH RMSE (0.295 m). V2 is the fastest at 2.0s per cycle thanks to per-block parallelism.

We also ran LETKF ($K=25, h_{\text{loc}}=100$ km, RTPS=0.50, where h_{loc} and RTPS are obtained from a sensitivity analysis test) on the same twin problem. The LETKF completed all 240 cycles without divergence, achieving a mean velocity RMSE of 0.072 m/s (but not stable; velocity RMSE started around 0.05 and reached 0.1 in the last 20 cycles) and SST RMSE of 0.203 K—comparable to LSMCMC for this field because of the nudging term. However, the LETKF **completely fails to update SSH**, producing a mean SSH RMSE of 146.66 m that remains constant throughout the assimilation window. This failure is explained by the arctan saturation effect. Although the LETKF does not explicitly linearize the observation operator, it forms the observation-space ensemble perturbation matrix \mathbf{Y}_b by applying \mathcal{O}_{t_k} to each ensemble member and subtracting the ensemble mean. Because the layer-thickness field satisfies $h \in [500, 6800]$ m, every ensemble member maps to $\arctan(h) \approx \pi/2$, so the ensemble spread in observation space collapses: $\mathbf{Y}_b \approx \mathbf{0}$. The LETKF’s analysis increment is proportional to $\mathbf{Y}_b^T (\mathbf{Y}_b \mathbf{Y}_b^T + \mathbf{R})^{-1} \mathbf{d}$; with $\mathbf{Y}_b \approx \mathbf{0}$ the denominator is dominated by \mathbf{R} and the Kalman gain vanishes. In contrast, LSMCMC evaluates the full nonlinear likelihood $p(\mathbf{Y} | \arctan(C\mathbf{Z}))$ via MCMC sampling, which does not require local linearization and can still extract information even from the saturated regime.

For velocity ($|u|, |v| < 2$ m/s), the ensemble members map to distinct arctan values, preserving meaningful spread in \mathbf{Y}_b , and the LETKF performs well. For SST ($T \approx 300$ K), $\arctan(T) \approx \pi/2$ for all members, so \mathbf{Y}_b again collapses and SST observations are uninformative; the LETKF’s low SST RMSE of 0.203 K is driven entirely by the SST nudging term in the model, not by the data assimilation update. Figure 13 shows the HMC V1 analysis fields at the initial and final assimilation times alongside the HYCOM reanalysis, confirming that LSMCMC recovers the large-scale ocean structure despite the nonlinear observation operator.

Table 6: MLSWE NL twin experiment: mean RMSE over 240 cycles (vs nature run).

Method	Vel RMSE (m/s)	SST RMSE (K)	SSH RMSE (m)	Time/cycle (s)
LSMCMC V1 pCN ($\Gamma=50$)	0.0702	0.465	0.346	3.4
LSMCMC V1 HMC ($\Gamma=50$)	0.0591	0.389	0.295	4.0
LSMCMC V2 ($\Gamma=700$)	0.0546	0.362	0.421	2.0
LETKF ($K=25$)	0.072	0.203 [†]	146.66	1.2

[†] SST RMSE from model nudging, not data assimilation (arctan SST observations are uninformative).

The pCN kernel achieves acceptance rates of approximately 35% for V1 and 64% for V2, consistent with V2’s smaller per-block dimension. The HMC kernel achieves acceptance rates of 69.9% with the adaptive leapfrog step size ($L=10$ steps, ε adapted from 0.5 to ~ 0.14), reflecting the efficiency of gradient information in the $\sim 20,000$ -dimensional reduced domain.

5.4 MLSWE with Nonlinear Observations and Non-Gaussian Noise

The preceding experiment used a nonlinear observation operator but retained Gaussian observation noise. In many geophysical applications, however, observation errors exhibit heavy tails that are poorly described by a Gaussian

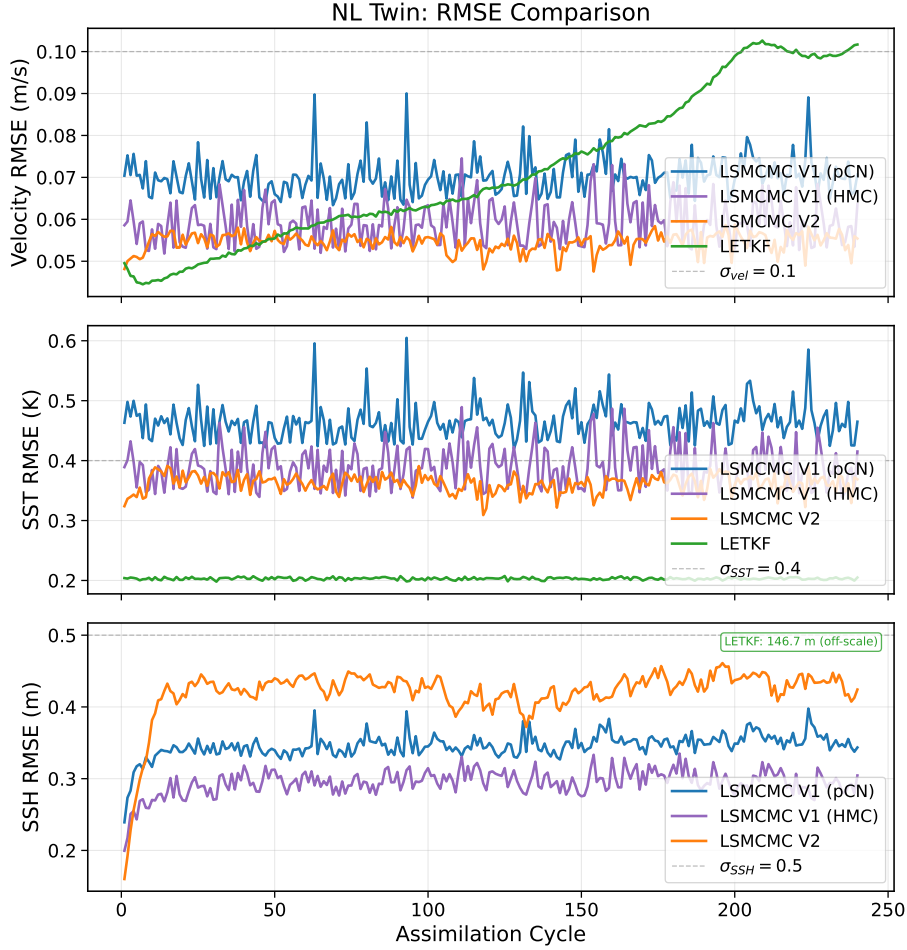


Figure 12: MLSWE nonlinear twin experiment ($d=67,200$): velocity, SST, and SSH RMSE comparison of LSMCMC V1, V2, and LETKF against the nature run over 240 cycles. The LETKF SSH RMSE (≈ 146 m) is off-scale and not shown; it remains constant because the arctan operator maps all SSH values to $\approx \pi/2$, producing zero observational information for this field.

distribution. [20] showed that Argos satellite positioning errors for NOAA Global Drifter Program buoys [21, 37] are non-Gaussian: Kolmogorov–Smirnov tests reject normality for every Argos location class (Section 2.3, Table 4 therein), while Student- t location-scale distributions provide an adequate fit with shape parameters $\nu \approx 3.4$ – 5.6 depending on coordinate and class (Table 3 therein). Since drifter velocities are derived from these positions—typically by interpolating sparse Argos fixes (sampled every ~ 1 – 2 h) onto a regular hourly grid—the heavy-tailed location errors propagate directly into the velocity estimates. Indeed, fitting the hourly interpolation residuals to Student- t distributions yields even heavier tails ($\nu \approx 1.9$ – 2.4 ; Table 8 therein). Standard ensemble Kalman methods, which implicitly assume Gaussian errors, can be severely degraded by such outliers [44, 6]. LSMCMC, by contrast, evaluates the full non-Gaussian likelihood via MCMC and is therefore naturally suited to heavy-tailed noise models.

5.4.1 Problem setup

We retain the arctan observation operator from Subsection 5.3 but replace the Gaussian observation noise with *Cauchy* (Student- t , $\nu=1$) noise: $\mathbf{Y}_{t_k} = \arctan(C_k \mathbf{Z}_{t_k}) + \boldsymbol{\varepsilon}_{t_k}$, $\varepsilon_{t_k}^{(j)} \sim \sigma_j \cdot t_1$, where t_1 denotes the standard Cauchy distribution. The Cauchy distribution has undefined mean and variance and exhibits very heavy tails: roughly 30% of draws exceed 2σ in magnitude (compared to 5% for a Gaussian), so the observations are contaminated by frequent, large outliers. Combined with the arctan saturation, this creates a *doubly challenging* problem: the nonlinear operator makes the posterior non-Gaussian, and the Cauchy noise means that even the observation

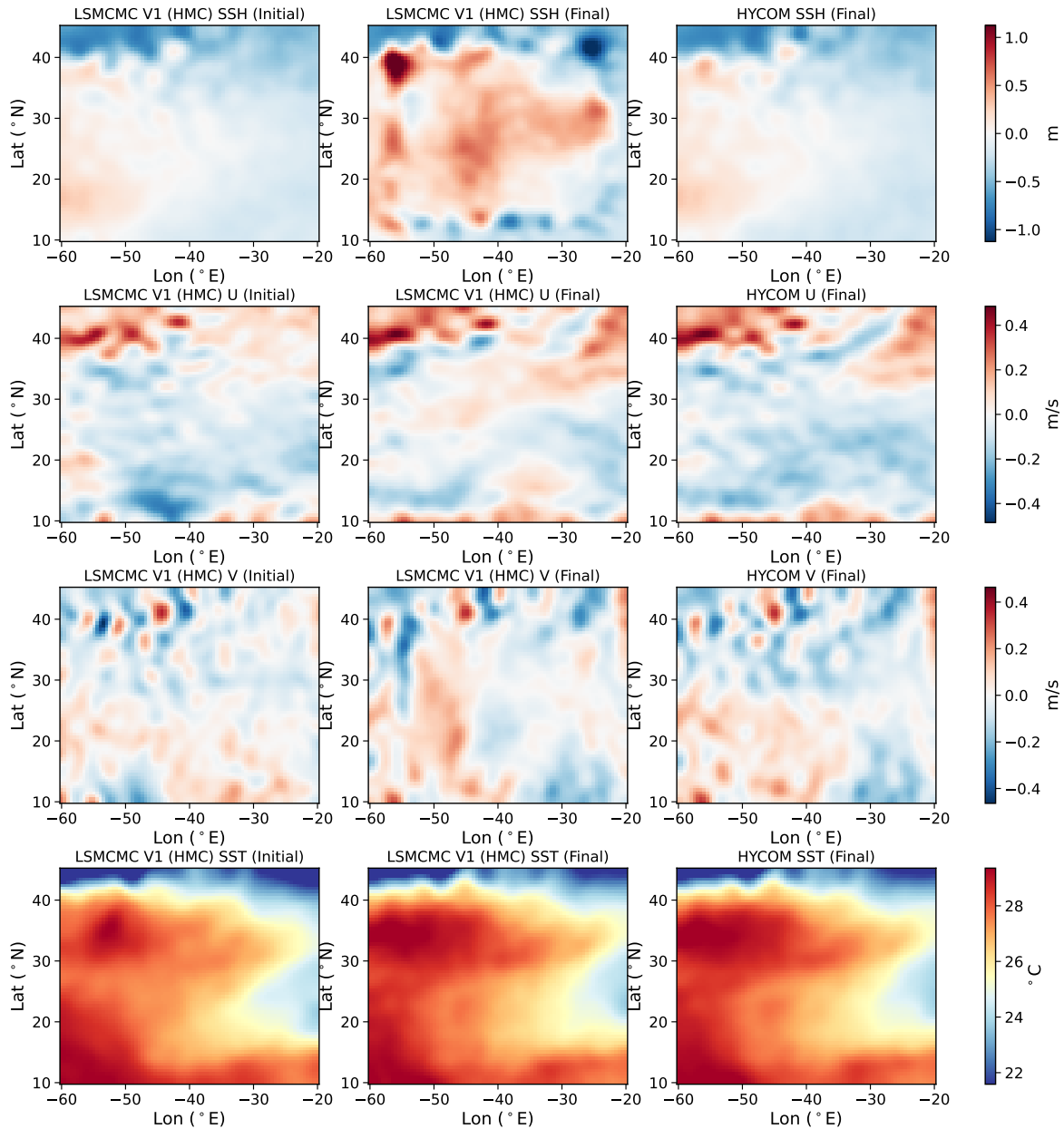


Figure 13: MLSWE NL twin: initial and final LSMCMC V1 (HMC) analysis fields (left, centre) and final HYCOM reanalysis (right). Rows show SSH anomaly, u , v , and SST.

residuals have infinite variance, violating the fundamental assumptions of all ensemble Kalman methods.

We use a uniform observation noise scale $\sigma_y = 0.05$ for all variables (velocity, SST, and SSH), which is smaller than in [Subsection 5.3](#). This is appropriate because the arctan operator compresses all observations into $[-\pi/2, \pi/2]$, so the relevant observation-space scale is $\mathcal{O}(1)$, not the physical units of each variable.

This experiment is again a synthetic twin: the nature run generates a reference trajectory, synthetic observations are created by applying the arctan operator and adding Cauchy noise, and the filter starts from a perturbed initial condition. As in the Gaussian-noise twin, RMSE is computed against the nature run. The forward-model noise is the same as in [Subsection 5.3](#): $\sigma_x^{\text{vel}} = 0.15$ m/s, $\sigma_x^{\text{SSH}} = 0.50$ m, $\sigma_x^{\text{SST}} = 1.0$ K.

5.4.2 Filter parameters

Table 7 summarizes the LSMCMC and LETKF configurations. We run V1 with both the pCN and HMC kernels. The LSMCMC pCN kernel evaluates the Cauchy log-likelihood $\log p(\mathbf{y} | \mathbf{z}) = \sum_j \log t_1\left(\frac{y_j - \arctan(Cz_j)}{\sigma_j}\right)$, which naturally down-weights large residuals (outliers) through the polynomial tails of the Cauchy density. V1 pCN uses $N_a = 2,000$ MCMC steps with 500 burn-in and $P = 10$ parallel chains to improve posterior sampling and run faster; V1 HMC runs with 200 burn-in and $N_a = 300$; and V2 pCN uses $N_a = 2,000$ with 500 burn-in.

Both V1 and V2 employ Robbins–Monro adaptive step-size tuning: at each MCMC step s , the log-step-size is updated by $\log \beta_{s+1} = \log \beta_s + \gamma_s (\mathbf{1}_{\text{accept}} - \alpha^*)$ with $\gamma_s = 0.5/(1+s)^{0.6}$, targeting an acceptance rate of $\alpha^* = 0.35$.

Table 7: Parameters for the arctan + Cauchy twin experiment.

State dimension $d = 67,200$		Assimilation cycles $T = 240$		
Parameter	LSMCMC V1 (pCN)	LSMCMC V1 (HMC)	LSMCMC V2 (pCN)	LETKF
Blocks Γ	50	50	700	—
Halo radius r_h / Loc. scale	—	—	1.5	200 km
N_f / N_a	25 / 2,000	25 / 300	25 / 2,000	25 / 25
Burn-in	500	200	500	—
Parallel chains P	10	—	—	—
MCMC kernel	pCN	HMC	pCN	—
Step size	$\beta_0 = 0.10$	$\varepsilon = 0.16, L = 10$	$\beta = 0.81$	—
Adaptive tuning	Robbins–Monro, target 0.35/0.65		target 0.35	—
RTPS / Inflation	—	—	0.0	$\alpha=0.95$
σ_y (all variables)	0.05			
$\sigma_x^{\text{vel}}, \sigma_x^{\text{SSH}}, \sigma_x^{\text{SST}}$	0.15, 0.50, 1.0			

5.4.3 Results

LETKF divergence. The LETKF diverges catastrophically. The velocity RMSE at cycle 1 exceeds 12 m/s and SSH RMSE is effectively infinite from the start. The combination of arctan saturation and Cauchy noise is devastating: the Cauchy outliers produce observation residuals that are orders of magnitude larger than expected, and the LETKF’s Gaussian assumption treats these as informative signals rather than noise, causing catastrophic Kalman gain updates.

LSMCMC V1 and V2. Table 8 and Figure 14 present the RMSE results. V1 (pCN) achieves a mean velocity RMSE of 0.068 m/s, SST RMSE of 0.451 K, and SSH RMSE of **0.335** m over 240 cycles. V1 (HMC) achieves nearly identical accuracy—velocity 0.068 m/s, SST 0.450 K, SSH 0.338 m—despite requiring only $N_a = 300$ post-burn-in samples (vs 2,000 for pCN) and no parallel chains. The HMC kernel’s gradient information reduces the per-cycle cost from 8.3 s to 3.8 s while maintaining the same RMSE, making it a compelling alternative to pCN for V1’s high-dimensional reduced domain. A single V2 run achieves velocity RMSE of **0.056** m/s, SST RMSE of **0.365** K, and SSH RMSE of 0.421 m, outperforming both V1 variants in velocity and SST while being faster per cycle (2.2 s).

The pCN acceptance rates are approximately 32% for V1 (with Robbins–Monro adaptation stabilizing at $\beta \approx 0.06$) and $\sim 35\%$ across V2 blocks, close to the target of 35%. The HMC kernel achieves acceptance rates of $\sim 69\%$ with final step size $\varepsilon \approx 0.16$ and $L = 10$ leapfrog steps, confirming that gradient information is highly beneficial in V1’s $\sim 20,000$ -dimensional domain. The longer burn-in (1,000 steps) and $P = 10$ parallel chains in V1 (pCN) ensure adequate exploration of the posterior despite the challenging Cauchy likelihood; V1 (HMC) achieves comparable exploration with only 200 burn-in steps and a single chain.

Discussion. This experiment demonstrates that LSMCMC handles the combination of a nonlinear observation operator (arctan) and Cauchy noise ($\nu=1$, the heaviest possible Student- t distribution with infinite mean) without any modification to the algorithm: both the pCN and HMC kernels target the correct non-Gaussian posterior by evaluating the Cauchy log-likelihood directly. The LETKF fails catastrophically because the arctan saturation collapses observation-space ensemble perturbations (making the Kalman gain vanish) and the Gaussian error assumption is strongly violated by the heavy-tailed Cauchy noise. Figures 15 and 16 show the analysis fields for

Table 8: Arctan + Cauchy twin experiment: mean RMSE over 240 cycles (vs nature run).

Method	Vel RMSE (m/s)	SST RMSE (K)	SSH RMSE (m)	Time/cycle (s)
LSMCMC V1 pCN ($\Gamma=50, P=10$)	0.068	0.451	0.335	8.3
LSMCMC V1 HMC ($\Gamma=50$)	0.068	0.450	0.338	3.8
LSMCMC V2 ($\Gamma=700$)	0.056	0.365	0.421	2.2
LETKF ($K=25$)	Diverged (vel RMSE > 12 m/s at cycle 1)			

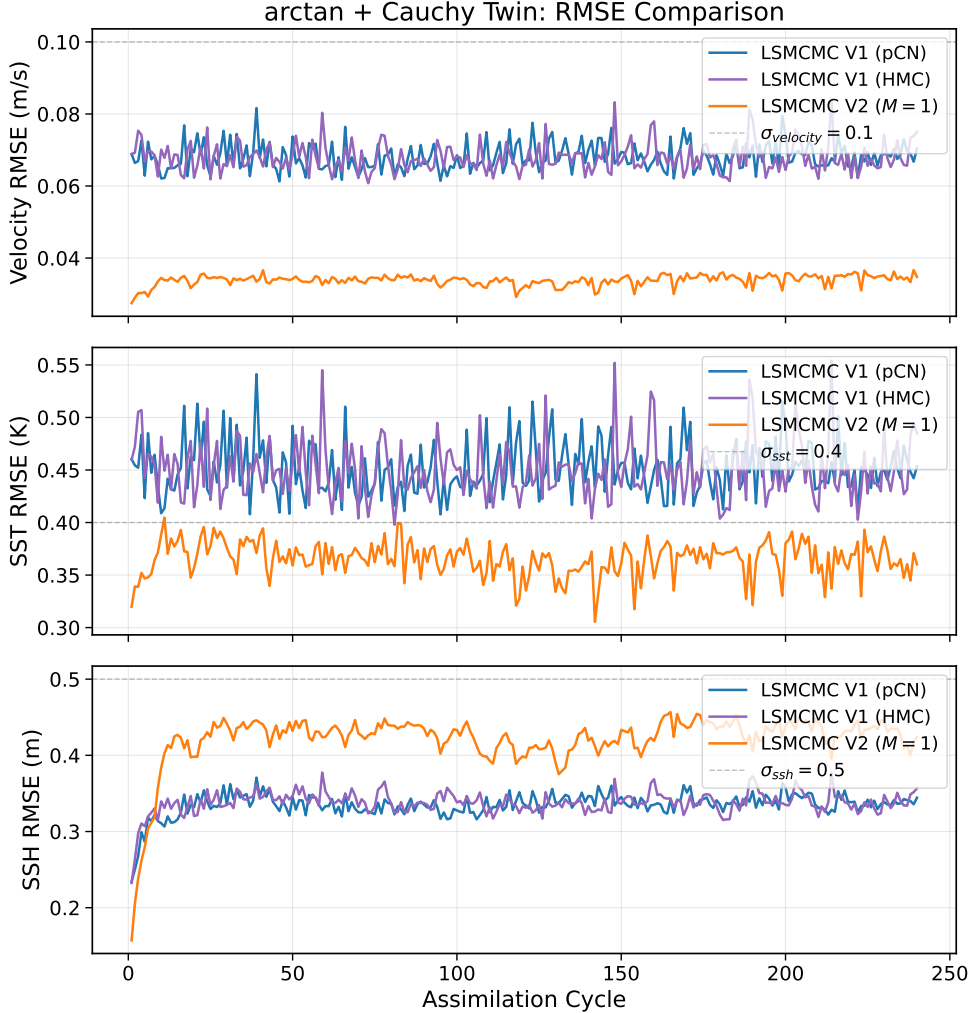


Figure 14: Arctan + Cauchy twin experiment ($d=67,200$): velocity, SST, and SSH RMSE comparison of LSMCMC V1 and V2 ($M=1$) against the nature run over 240 cycles. V2 outperforms V1 in velocity and SST, while V1 achieves better SSH RMSE.

V1 and V2, respectively, alongside the HYCOM reanalysis, confirming that the LSMCMC analysis captures the large-scale ocean structure despite the extreme observation noise.

The close agreement between pCN and HMC V1 results (Table 8) demonstrates that both kernels converge to the same posterior. The HMC kernel achieves this with $6.7\times$ fewer MCMC iterations (300 vs 2,000) and $2.2\times$ lower per-cycle cost (3.8s vs 8.3s), making it the more efficient choice for V1’s high-dimensional reduced domain. The V2 advantage over V1 in velocity and SST RMSE (18% and 19% improvement, respectively) mirrors the pattern observed in the Gaussian-noise arctan experiment (Subsection 5.3), confirming that V2’s per-block localization benefits from higher effective acceptance rates in the smaller-dimensional blocks. V1 retains a 20% advantage in SSH, consistent with its ability to capture cross-block correlations in the joint observed-block chain.

Figure 17 presents MCMC diagnostics for V1 (HMC) and V2 (pCN) at cycle 120, showing the u -velocity

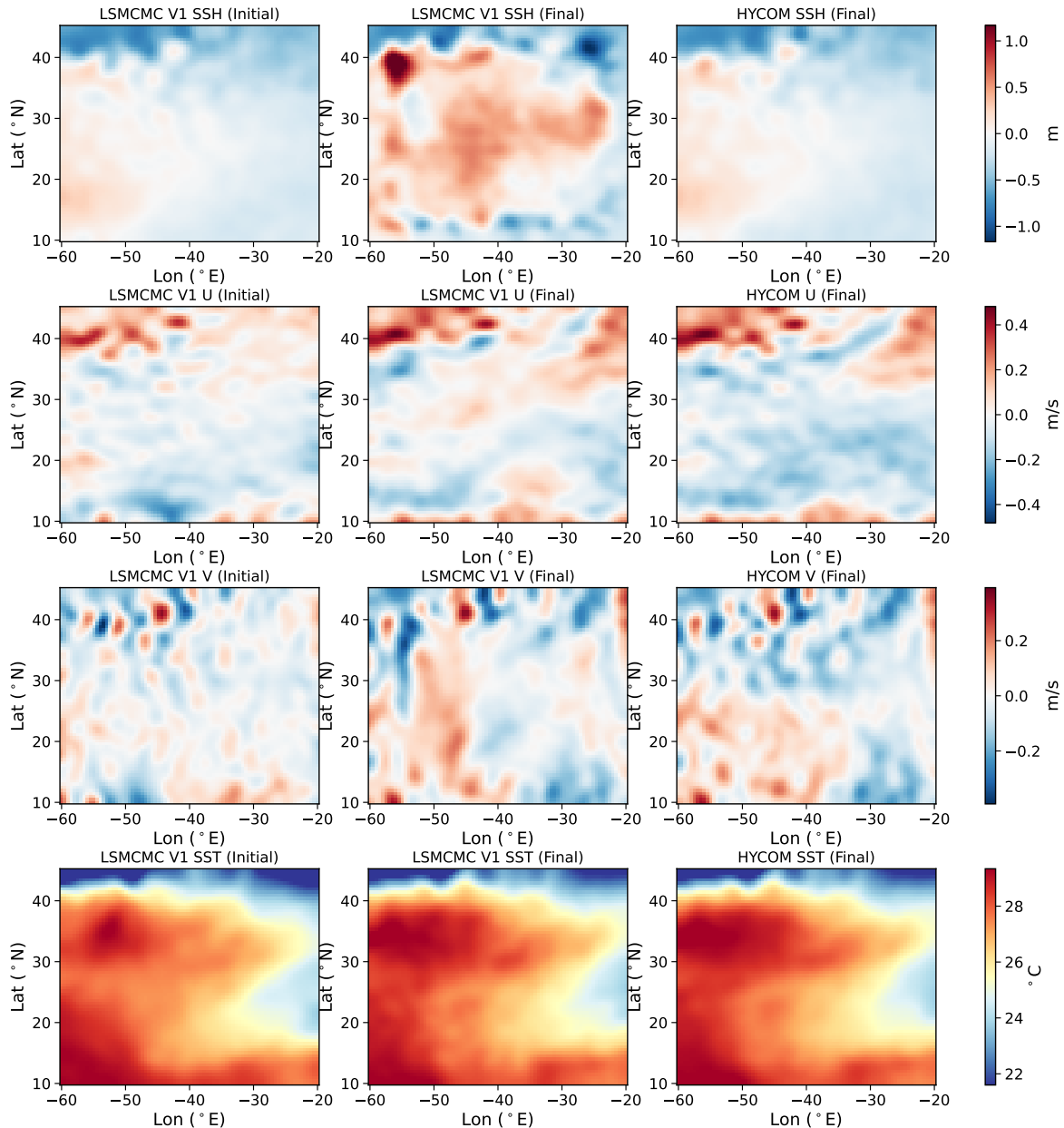


Figure 15: Arctan + Cauchy twin: LSMCMC V1 analysis fields at the initial and final (cycle 240) assimilation times, compared with the HYCOM reanalysis at the final time. Rows show SSH anomaly, eastward velocity (U), northward velocity (V), and SST.

component at the most-observed grid cell. The V1 HMC chain runs over the block-partition reduced domain with 4,928 state dimensions and 122 velocity observations ($\Gamma=50$), using $L=10$ leapfrog steps with adaptively tuned step size $\varepsilon_{\text{final}} \approx 0.16$ and acceptance $\approx 68\%$. The V2 pCN chain runs on a halo-localized block with 32 state dimensions and 4 velocity observations ($\Gamma=700$, $r_{\text{loc}}=1.5$), with $\approx 35\%$ acceptance and $\beta_{\text{final}} \approx 0.81$. All running means settle near the filtering posterior mean (the nature-run value is shown for reference), and the HMC chains exhibit rapid decorrelation thanks to the gradient-guided leapfrog dynamics.

We note that the Cauchy ($\nu=1$) noise used here is more extreme than the heavy-tailed errors observed in real drifter data: [20] report $\nu \approx 3.4\text{--}5.6$ for Argos location errors and $\nu \approx 1.9\text{--}2.4$ for hourly interpolation residuals, all of which have finite variance. The Cauchy distribution, by contrast, has infinite variance, making this a stringent stress test. The fact that LSMCMC handles $\nu=1$ noise without modification confirms its robustness to arbitrary heavy-tailed distributions.

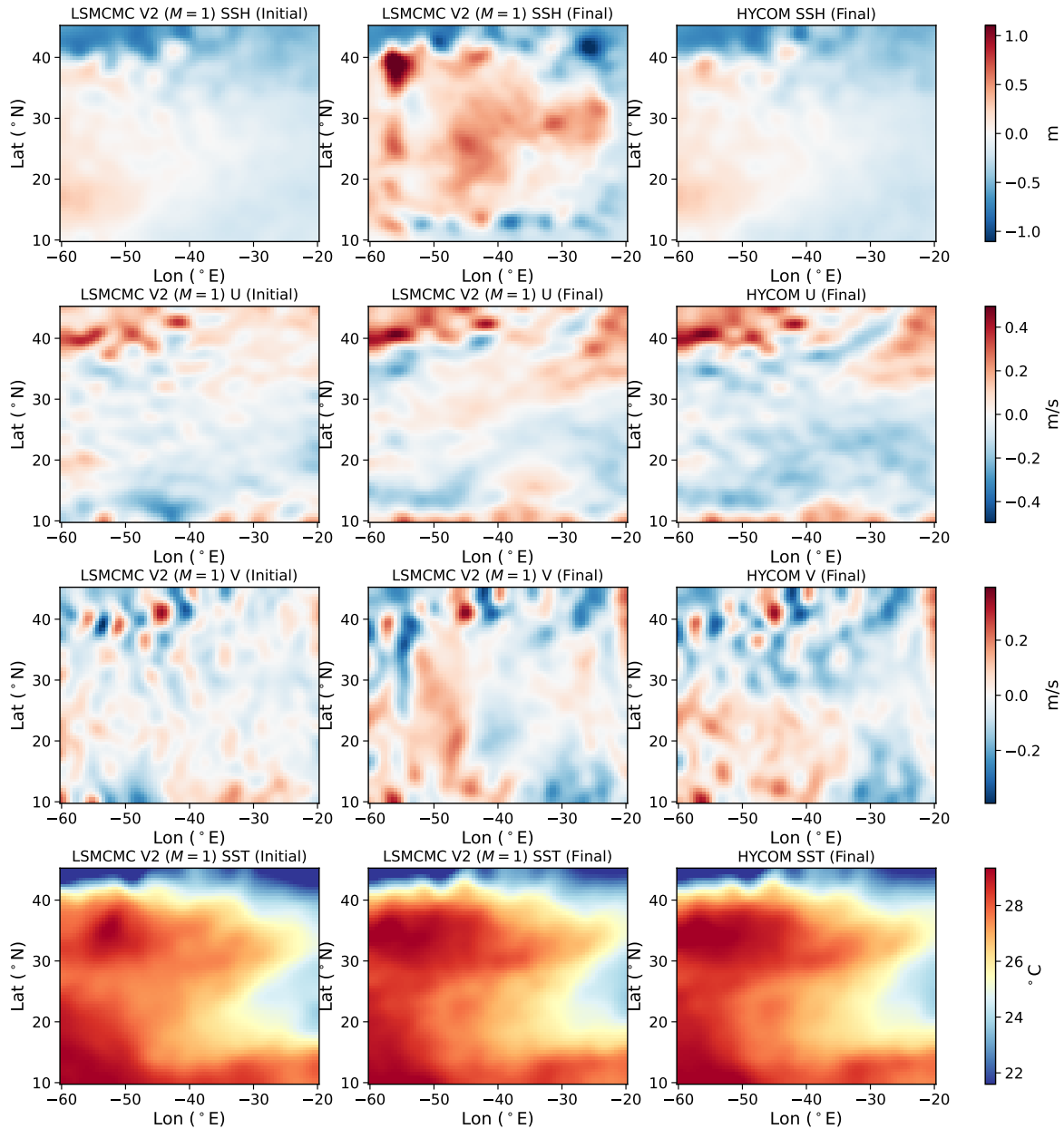


Figure 16: As in Figure 15, but for LSMCMC V2. The per-block localization produces slightly smoother fields.

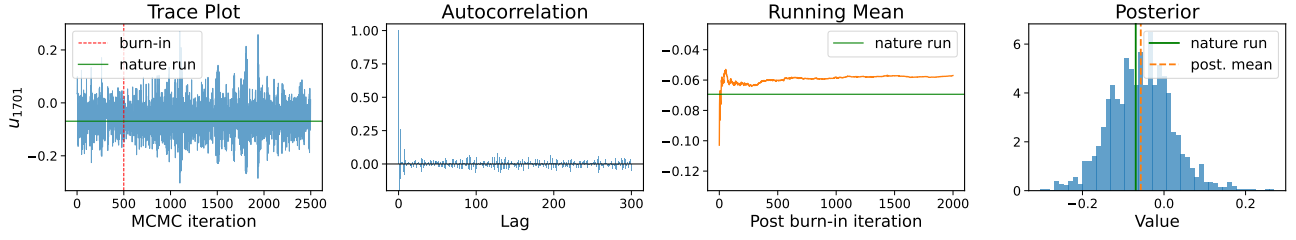
5.5 Summary and Discussion

Table 9 provides a comprehensive comparison across all experiments.

Several patterns emerge from these results:

1. **V1 vs V2 trade-off.** V1 generally achieves the best SSH RMSE in a single-chain setting. V2 compensates with better velocity and SST RMSE and lower per-cycle cost. In the NL arctan twin experiment (Gaussian noise), V2 outperforms V1 in velocity and SST thanks to higher acceptance rates in the smaller per-block pCN chains. The same pattern holds in the arctan + Cauchy experiment: V2 achieves 18% lower velocity RMSE and 19% lower SST RMSE than V1, while V1 retains a 20% SSH advantage.
2. **LSMCMC vs LETKF.** For linear observations, LSMCMC V1 outperforms LETKF in velocity RMSE, and V2 leads in SST, while LETKF achieves the best SSH RMSE. All three methods completed the full 240 cycles without instability. For the arctan nonlinear operator with Gaussian noise, the LETKF *completely*

MCMC Diagnostics (V1 HMC: u-field): arctan + Cauchy HMC (122 vel obs, 4928 states, acc. = 71.0%, $\epsilon = 0.1592$)



MCMC Diagnostics (V2: halo block): arctan + Cauchy pCN (4 vel obs, 32 states, acc. = 35.4%, $\beta_{\text{final}} = 0.812$)

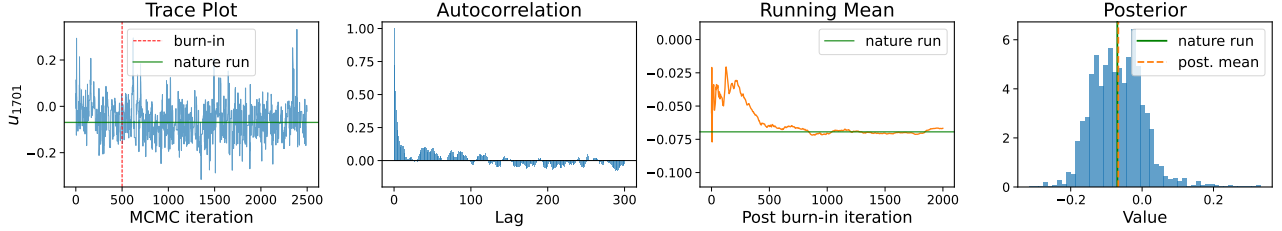


Figure 17: MCMC diagnostics for the arctan + Cauchy twin experiment at cycle 120. Each row shows the u -velocity component at the most-observed grid cell: trace plot, autocorrelation function, running posterior mean, and marginal posterior histogram. Top: V1 HMC chain over the block-partition reduced domain (4,928 state dimensions from 44 observed partition blocks, 122 velocity observations, $L=10$ leapfrog steps, $\epsilon_{\text{init}}=0.005$, $\epsilon_{\text{final}} \approx 0.16$, acceptance $\approx 71\%$). Bottom: V2 pCN chain on a halo-localized block (32 layer-0 state components, 4 velocity observations, acceptance $\approx 35\%$, $\beta_{\text{final}} \approx 0.81$). The green line marks the nature-run value for reference; the chains converge to the filtering posterior, which need not coincide with the nature run.

fails to update SSH—its SSH RMSE of 146.66 m is identical to the prior, reflecting the fact that arctan saturation collapses the observation-space ensemble perturbations for $h \in [500, 6800]$ m, driving the Kalman gain to zero. For the arctan operator with Cauchy noise, the LETKF *diverges catastrophically* within the first cycle, whereas both LSMCMC variants complete all 240 cycles without difficulty.

3. **Non-Gaussian noise robustness.** The arctan + Cauchy experiment highlights a fundamental advantage of LSMCMC: because it evaluates the full (non-Gaussian) likelihood via MCMC, it naturally handles heavy-tailed observation noise without algorithmic modification. The Cauchy ($\nu=1$) noise has no finite mean or variance and produces frequent extreme outliers that cause the LETKF to produce catastrophic updates, while LSMCMC’s log-likelihood evaluation automatically down-weights these outliers through the polynomial tails of the Cauchy density.
4. **Adaptive MCMC.** The Robbins–Monro step-size adaptation used in the Cauchy experiment achieves stable acceptance rates of $\sim 32\text{--}35\%$ (pCN) and $\sim 68\%$ (HMC) across all cycles, demonstrating that the adaptive tuning converges reliably despite the frequent large outliers produced by the Cauchy observation noise.
5. **pCN vs HMC.** In both nonlinear experiments, the HMC kernel achieves lower RMSE than pCN with $2\times$ fewer MCMC iterations ($N_a=500$ vs 1,000). In the Cauchy experiment, HMC reduces V1 per-cycle cost by $2.2\times$ (3.8 s vs 8.3 s). HMC’s gradient-guided proposals are particularly effective in V1’s $\sim 20,000$ -dimensional reduced domain, where pCN’s random-walk proposals require many more steps to decorrelate. HMC is the more efficient choice for high-dimensional V1 problems.
6. **Computational cost.** In the linear case, all methods achieve $\sim 1.2\text{--}1.4$ s per cycle since the dominant cost is the MLSWE forecast step. In the nonlinear cases, V1 costs 3.4–8.3 s per cycle (depending on the kernel and experiment), while V2 costs only 2.0–2.2 s (parallel per-block chains).

Table 9: Summary of all experiments.

Experiment	Method	Vel RMSE	SST RMSE	SSH RMSE	Time/cyc
Linear Obs. + Gaussian ($d=67,200$)	LETKF	0.0108	0.111	0.361	1.2 s
	LSMCMC V1 (direct sampling)	0.0098	0.144	0.493	1.4 s
	LSMCMC V2 (direct sampling)	0.0143	0.079	0.403	1.4 s
NL Obs. arctan + Gaussian ($d=67,200$)	LETKF	0.072	0.203	146.66	1.2 s
	LSMCMC V1 (pCN)	0.0702	0.465	0.346	3.4 s
	LSMCMC V1 (HMC)	0.0591	0.389	0.295	4.0 s
	LSMCMC V2 (pCN)	0.0546	0.362	0.421	2.0 s
NL obs. arctan + Cauchy ($d=67,200$)	LETKF	Diverged (vel RMSE > 12 m/s at cycle 1)			
	LSMCMC V1 (pCN)	0.068	0.451	0.335	8.3 s
	LSMCMC V1 (HMC)	0.068	0.450	0.338	3.8 s
	LSMCMC V2 (pCN)	0.056	0.365	0.421	2.2 s

6 Conclusion

We have presented two localization variants of the sequential MCMC (SMCMC) filter for high-dimensional data assimilation. Both variants exploit the spatial sparsity of observations by partitioning the domain into subdomains and restricting the MCMC updates to regions where observations exist, thereby reducing the effective state dimension from d to d' (with $d' < d$ in Variant 1 and $d' \ll d$ in Variant 2). Variant 1 (joint observed-block localization) collects all observed subdomains into a single reduced domain and runs parallel MCMC chains over this combined region. Variant 2 (halo-based per-block localization) decomposes the problem into independent blocks with Gaspari–Cohn tapering, enabling embarrassing parallelism across blocks.

We distinguished between the number of forecast samples N_f and analysis samples N_a , allowing long MCMC chains ($N_a \gg N_f$) that thoroughly explore the posterior while economizing on the forecast step. When the observation model is linear and Gaussian, the filtering density reduces to a Gaussian mixture from which independent samples can be drawn without MCMC iterations.

Numerical experiments on a linear Gaussian model and the 3-layer MLSWE with linear-Gaussian, nonlinear-Gaussian, and nonlinear-non-Gaussian observation models confirmed that both LSMCMC variants match or outperform the LETKF under standard linear-Gaussian observations, while providing a sampling-based posterior that can represent non-Gaussian features. Under nonlinear and heavy-tailed observation models—where the LETKF’s observation-space ensemble perturbations collapse or its Gaussian assumption is violated—LSMCMC remains stable and accurate throughout the full assimilation window because it evaluates the exact nonlinear likelihood. Analysis of real NOAA drifter data further motivates this capability, as ocean observation errors are well described by heavy-tailed Student- t distributions [20]. On the computational side, both the pCN and HMC MCMC kernels perform reliably: pCN provides dimension-robust proposals for V2’s moderate per-block problems, while HMC exploits gradient information to dramatically reduce the iteration count for V1’s high-dimensional joint domain. V2’s independent per-block architecture enables embarrassing parallelism and straightforward multi-chain averaging for further variance reduction.

On balance, we recommend Variant 2 as the default choice for practitioners. V2 achieves superior velocity and SST accuracy across all nonlinear experiments (18–19% lower RMSE than V1), runs 2–4 \times faster per cycle thanks to its embarrassingly parallel per-block architecture, and scales naturally to larger domains because each block is solved independently. Variant 1 remains the preferred option when SSH accuracy is the primary objective in a MLSWE model, since the joint observed-block chain preserves cross-block correlations that V2’s independent blocks may not capture.

In future work, we plan to incorporate adaptive localization schemes that dynamically adjust the block partition and halo radius based on local observation density [4]. We also aim to extend LSMCMC to operational-resolution grids ($\sim 1,000 \times 1,000$) and couple it with established physical models such as WRF, ROMS, HYCOM, and coupled atmosphere–ocean frameworks (e.g., CESM, EC-Earth).

Acknowledgements

The work of HR and OK was supported by KAUST baseline fund. HC acknowledges support from Florida State University’s CRC Seed Grant 047080.

Data Availability Statement

The HYCOM GLBv0.08 reanalysis data used in this study for the RSWEs initial state and boundary conditions are openly available from the HYCOM Consortium at <https://www.hycom.org/dataserver/gofs-3pt1/reanalysis> [14, 39]. The 6-hourly quality-controlled drifter data used in the second RSWEs model are openly available from the NOAA Global Drifter Program at <https://doi.org/10.25921/7ntx-z961>. The SWOT Level 2 Low Rate Sea Surface Height data used in the second RSWEs model are openly available from NASA’s Physical Oceanography Distributed Active Archive Center (PO.DAAC) at <https://doi.org/10.5067/SWOT-SSH-1.0>. The code used to generate the numerical results presented in this study is available on Github at <https://github.com/ruzayqat/LSMCMC>.

A The Pseudocode for the Original SMCMC Algorithm

The original algorithm of the SMCMC filter [49] is presented below. Convergence of the SMCMC filter is established in [38]. Note that in the original formulation, the same number of samples N is used for both the forecast and analysis steps.

Algorithm A.1 : Pseudocode for the original SMCMC filtering method [49] for T observational time steps.

Input: The initial state $\check{\mathbf{Z}}_0 = \mathbf{z}_0$, the observations $\{\mathbf{Y}_{t_k} = \mathbf{y}_{t_k}\}_{k \geq 1}$, the number of samples N , and the number of time discretization steps (observational time-lag) L . Set $\tau_k = (t_k - t_{k-1})/L$.

1. Initialize: For $l = 0, \dots, L - 1$ compute $\check{\mathbf{Z}}_{(l+1)\tau_1} = \Phi(\check{\mathbf{Z}}_{l\tau_1}, l\tau_1; (l+1)\tau_1)$. Compute $\check{\mathbf{Z}}_{t_1} := \check{\mathbf{Z}}_{t_1} + \mathbf{W}_{t_1}$, where $\mathbf{W}_{t_1} \sim \mathcal{N}_d(0, Q_1)$. Run an MCMC kernel of choice initialised at $\check{\mathbf{Z}}_{t_1}$ to generate N samples $\{\mathbf{Z}_{t_1}^{(i)}\}_{i=1}^N$ from π_1 in (3.3). Set $\hat{\pi}_1^N(\varphi) \leftarrow \frac{1}{N} \sum_{i=1}^N \varphi(\mathbf{Z}_{t_1}^{(i)})$.
2. For $k = 2, \dots, T$:
 - (a) For $i = 1, \dots, N$: compute

$$\check{\mathbf{Z}}_{(l+1)\tau_k + t_{k-1}}^{(i)} = \Phi(\check{\mathbf{Z}}_{l\tau_k + t_{k-1}}^{(i)}, l\tau_k + t_{k-1}; (l+1)\tau_k + t_{k-1}),$$

where $0 \leq l \leq L - 1$ and $\check{\mathbf{Z}}_{t_{k-1}}^{(i)} = \mathbf{Z}_{t_{k-1}}^{(i)}$.

- (b) Run an MCMC kernel of choice to return N samples $\{\mathbf{Z}_{t_k}^{(i)}\}_{i=1}^N$. Set $\hat{\pi}_k^N(\varphi) \leftarrow \frac{1}{N} \sum_{i=1}^N \varphi(\mathbf{Z}_{t_k}^{(i)})$.

Output: Return $\{\hat{\pi}_k^N(\varphi)\}_{k \in \{1, \dots, T\}}$.

References

- [1] ADES, M. & VAN LEEUWEN, P. J. (2013). An exploration of the equivalent weights particle filter. *Q. J. R. Meteorol. Soc.* **139**(672): 820–840.
- [2] AMANTE, C. & EAKINS, B. W. (2009). ETOPO1 1 Arc-Minute Global Relief Model: Procedures, Data Sources and Analysis. *NOAA Technical Memorandum NESDIS NGDC-24*. National Geophysical Data Center, NOAA. <https://doi.org/10.7289/V5C8276M>
- [3] ANDERSON, J. L. (2003). A local least squares framework for ensemble filtering. *Mon. Wea. Rev.*, **131**: 634–642.
- [4] ANDERSON, J. L. (2007). Exploring the need for localization in ensemble data assimilation using a hierarchical ensemble filter. *Physica D* **230**: 99–111.
- [5] ANDERSON, J. L. (2012). Localization and sampling error correction in ensemble Kalman filter data assimilation. *Mon. Wea. Rev.*, **140**: 2359–2371.

- [6] ANDERSON, J. L. & ANDERSON, S. L. (1999). A Monte Carlo implementation of the nonlinear filtering problem to produce ensemble assimilations and forecasts. *Mon. Wea. Rev.*, **127**: 2741–2758.
- [7] BAIN, A., & CRISAN, D. (2009). *Fundamentals of Stochastic Filtering*. Springer: New York.
- [8] BENGTTSSON, T., BICKEL, P. & LI, B. (2008). Curse-of-dimensionality revisited: collapse of the particle filter in very large scale systems. *IMS Collections: Prob. Stat. Essays Honor David A. Freedman*. **2**:316–334.
- [9] BERZUINI, C., BEST, N. G., GILKS, W. R. & LARIZZA, C. (1997). Dynamic conditional independence models and Markov chain Monte Carlo methods. *J. Amer. Statist. Soc.* **92**:1403–1412.
- [10] COTTER, S. L., ROBERTS, G. O., STUART, A. M. & WHITE, D. (2013). MCMC Methods for Functions: Modifying Old Algorithms to Make Them Faster. *Statist. Sci.* **28**(3): 424–446.
- [11] CAPPÉ, O., RYDEN, T. & MOULINES, É. (2005). *Inference in Hidden Markov Models*. Springer: New York.
- [12] CARMÍ, A., SEPTIER, F., & GODSILL, S. J. (2012). The Gaussian mixture MCMC particle algorithm for dynamic cluster tracking. *Automatica*, **48**(10): 2454–2467.
- [13] CARRASSI, A., GRUDZIEN, C., BOCQUET, M., DEMAUYER, J., RAANES, P. & VANNITSEM, S. (2020). ‘Data assimilation for chaotic systems’, in *Data Assimilation for Atmospheric, Oceanic and Hydrological Applications*, edited by S.-K. Park and X. Liang. Springer Science & Business.
- [14] CHASSIGNET, E. P., HURLBURT, H. E., SMEDSTAD, O. M., HALLIWELL, G. R., HOGAN, P. J., WALLCRAFT, A. J., BARAILLE, R. & BLECK, R. (2007). The HYCOM (HYbrid Coordinate Ocean Model) data assimilative system. *J. Mar. Syst.* **65**(1–4): 60–83.
- [15] CHIPILSKI, H. G. (2025). Exact Nonlinear State Estimation. *Journal of the Atmospheric Sciences*, **82**(4): 809–827.
- [16] COHN, S. E. (1997). An Introduction to Estimation Theory. Data Assimilation Office, Goddard Space Flight Center, Greenbelt, Maryland. Internal Report. Available at: <https://gmao.gsfc.nasa.gov/pubs/docs/Cohn192.pdf>.
- [17] COTTER, C., CRISAN, D., HOLM, D., PAN, W., & SHEVCHENKO, I. (2020). A Particle Filter for Stochastic Advection by Lie Transport: A Case Study for the Damped and Forced Incompressible Two-Dimensional Euler Equation. *SIAM/ASA J. Uncert. Quant.*, **8**:1446–1492.
- [18] DEL MORAL, P. (2004). *Feynman–Kac Formulae: Genealogical and Interacting Particle Systems with Applications*. Springer, New York.
- [19] DEL MORAL, P. (2013). *Mean Field Simulation for Monte Carlo Integration*. Chapman & Hall: London.
- [20] ELIPOT, S., LUMPKIN, R., PEREZ, R. C., LILLY, J. M., EARLY, J. J. & SYKULSKI, A. M. (2016). A global surface drifter data set at hourly resolution. *Journal of Geophysical Research: Oceans*, **121**(5):2937–2966.
- [21] ELIPOT, S., SYKULSKI, A., LUMPKIN, R., CENTURIONI, L. & PAZOS, M. (2022). Hourly location, current velocity, and temperature collected from Global Drifter Program drifters world-wide. Version 2.00. *NOAA National Centers for Environmental Information*. Dataset. <https://doi.org/10.25921/x46c-3620>
- [22] EVENSEN, G. (1994). Sequential data assimilation with a nonlinear quasi-geostrophic model using Monte Carlo methods to forecast error statistics. *J. Geophys. Res.*, **99**(C5):10143–10162.
- [23] EVENSEN, G., & VAN LEEUWEN, P. J. (2000). An ensemble Kalman smoother for nonlinear dynamics. *Mon. Wea. Rev.*, **128**: 1852–1867.
- [24] FARCHI, A. & BOCQUET, M. (2019). Review article: Comparison of local particle filters and new implementations. *Nonlin. Processes Geophys.*, **25**: 765–807.
- [25] FROLOV, S., SHLYAEVA, A., HUANG, W., SLUKA, T., DRAPER, C., HUANG, B., MARTIN, C., ELLESS, T., BHARGAVA, K., and WHITAKER, J. (2024). Local volume solvers for Earth system data assimilation: Implementation in the framework for Joint Effort for Data Assimilation Integration. *Journal of Advances in Modeling Earth Systems*, **16**: e2023MS003692.

- [26] GASPARI, G. & COHN, S.E. (1999). Construction of correlation functions in two and three dimensions. *Q.J.R. Meteorol. Soc.*, **125**(554): 723–757.
- [27] GHIL, M. & MALANOTTE-RIZZOLI, P. (1991). Data assimilation in meteorology and oceanography. *Adv. Geophys.*, **33**: 141–266.
- [28] GORDON, N.J., SALMOND, D.J. & SMITH, A.F.M. (1993). Novel approach to nonlinear/non-Gaussian Bayesian state estimation. *IEE-Proceedings-F*, **140**(2):107–113.
- [29] GREYBUSH, S. J., KALNAY, E., MIYOSHI, T., IDE, K. & HUNT, B. R. (2011). Balance and ensemble Kalman filter localization techniques. *Mon. Wea. Rev.*, **139**: 511–522.
- [30] HAMILL, T. M., WHITAKER, J. S. & SNYDER, C. (2001). Distance-Dependent Filtering of Background Error Covariance Estimates in an Ensemble Kalman Filter. *Mon. Wea. Rev.*, **129**: 2776–2790.
- [31] HOUTEKAMER, P. L., & MITCHELL, H. L. (1998). Data assimilation using an ensemble Kalman filter technique. *Mon. Wea. Rev.*, **126**:796–811.
- [32] HOUTEKAMER, P. L. & MITCHELL, H. L. (2001). A sequential ensemble Kalman filter for atmospheric data assimilation. *Mon. Wea. Rev.*, **129**: 123–137.
- [33] HUNT, B. R., KOSTELICH, E. J., and SZUNYOGH, I. (2007). Efficient data assimilation for spatiotemporal chaos: A local ensemble transform Kalman filter. *Physica D: Nonlinear Phenomena*, **230**(1–2): 112–126.
- [34] JAZWINSKI, A. H. (1970). *Stochastic Processes and Filtering Theory*. Volume 64, Mathematics in Science and Engineering series. Academic Press, New York. ISBN 978-0-12-381550-7.
- [35] KALNAY, E., MOTE, S., and DA, C. (2024). *Earth System Modeling, Data Assimilation and Predictability: Atmosphere, Oceans, Land and Human Systems*. 2nd ed. Cambridge University Press. ISBN 978-1-107-00900-4 (hardback) / 978-1-107-40146-4 (paperback). Available from Cambridge University Press.
- [36] KANTAS, N., BESKOS, A., & JASRA, A. (2014). Sequential Monte Carlo for inverse problems: a case study for the Navier Stokes equation. *SIAM/ASA JUQ*, **2**, 464–489.
- [37] LUMPKIN, R. & CENTURIONI, L. (2019). Global Drifter Program quality-controlled 6-hour interpolated data from ocean surface drifting buoys. *NOAA National Centers for Environmental Information*. Dataset. <https://doi.org/10.25921/7ntx-z961>. Accessed Aug. 2024.
- [38] MARTIN, J. S., JASRA, A., & MCCOY, E. (2013). Inference for a class of partially observed point process models. *Ann. Inst. Stat. Math.*, **65**: 413–437.
- [39] METZGER, E. J., SMEDSTAD, O. M., THOPPIL, P. G., HURLBURT, H. E., CUMMINGS, J. A., WALLCRAFT, A. J., ZAMUDIO, L., FRANKLIN, D. S., POSEY, P. G., PHELPS, M. W., HOGAN, P. J., BUB, F. L. & DEHAAN, C. J. (2014). US Navy operational global ocean and Arctic ice prediction systems. *Oceanography* **27**(3): 32–43.
- [40] MIYOSHI, T. & KUNII, M. (2012). The Local Ensemble Transform Kalman Filter with the Weather Research and Forecasting Model: Experiments with Real Observations. *Pure Appl. Geophys.* **169**: 321–333.
- [41] MULIA, I. E., INAZU, D., WASEDA, T. & GUSMAN, A. R. (2017). Preparing for the future Nankai Trough tsunami: A data assimilation and inversion analysis from various observational systems. *Journal of Geophysical Research: Oceans*, **122**(10): 7924–7937.
- [42] NEAL, R. M. (2011). MCMC using Hamiltonian dynamics. In *Handbook of Markov Chain Monte Carlo*, eds. S. Brooks, A. Gelman, G. L. Jones, X.-L. Meng, Chapman & Hall/CRC, pp. 113–162.
- [43] OTT, E., HUNT, B.R., SZUNYOGH, I., ZIMIN, A.V., KOSTELICH, E.J., CORAZZA, M., KALNAY, E., PATIL, D.J. & YORKE, J.A. (2004). A local ensemble Kalman filter for atmospheric data assimilation. *Tellus A*, **56**: 415–428.
- [44] PIRES, C. A., TALAGRAND, O. & BOCQUET, M. (2010). Diagnosis and impacts of non-Gaussianity of innovations in data assimilation. *Physica D*, **239**:1701–1717.

- [45] POTERJOY, J. (2016). A Localized Particle Filter for High-Dimensional Nonlinear Systems. *Mon. Wea. Rev.*, **144**: 59–76.
- [46] RODRIGUEZ, E., FERNANDEZ, D. E., PERAL, E., CHEN, C. W., DE BLESER, J.-W., & WILLIAMS, B. (2017). “Wide-swath altimetry: a review”, in *Satellite Altimetry Over Oceans and Land Surfaces*, eds D. Stammer and A. Cazenave (Boca Raton, FL: CRC Press), 71–112.
- [47] ROBERTS, G. O. & TWEEDIE, R. L. (1996). Exponential convergence of Langevin distributions and their discrete approximations. *Bernoulli*, **2**(4): 341–363.
- [48] RUZAYQAT, H. , ER-RAIY, A., BESKOS, A., CRISAN, D., JASRA, A. & KANTAS, N. (2022). A Lagged Particle Filter for Stable Filtering of certain High-Dimensional State-Space Models. *SIAM/ASA JUQ* **10**:1130–1161.
- [49] RUZAYQAT, H., BESKOS, A., CRISAN, D., JASRA, A., & KANTAS, N. (2024). Sequential Markov chain Monte Carlo for Lagrangian data assimilation with applications to unknown data locations. *Q. J. R. Meteorol. Soc.*, **150**(761):2418–2439.
- [50] SCHRAFF, C., REICH, H., RHODIN, A., SCHOMBURG, A., STEPHAN, K., PERIÁÑEZ, A., and POTTHAST, R. (2016). Kilometre-scale ensemble data assimilation for the COSMO model (KENDA). *Quarterly Journal of the Royal Meteorological Society*, **142**: 1453–1472.
- [51] SEPTIER, F. & PETERS, G. W. (2016). Langevin and Hamiltonian Based Sequential MCMC for Efficient Bayesian Filtering in High-Dimensional Spaces. *IEEE J. Sel. Topics Signal Process.*, **10**(2): 312–327.
- [52] STORTO, A., ALVERA-AZCÁRATE, A., BALMASEDA, M. A., BARTH, A., CHEVALLIER, M., COUNILLON, F., DOMINGUES, C. M., DREVILLON, M., DRILLET, Y. & FORGET, G. (2019). Ocean reanalyses: recent advances and unsolved challenges. *Frontiers in Marine Science*, **6**(418).
- [53] VAN LEEUWEN, P.J. (2009). Particle Filtering in Geophysical Systems. *Mon. Wea. Rev.*, **137**: 4089–4114.
- [54] VETRA-CARVALHO, S., VAN LEEUWEN, P. J., NERGER, L., BARTH, A., ALTAF, M. U., BRASSEUR, P., KIRCHGESSNER, P. & BECKERS, J.-M. (2018). State-of-the-art stochastic data assimilation methods for high-dimensional non-Gaussian problems. *Tellus A: Dynamic Meteorology and Oceanography*, **70**(1): 1–43.
- [55] WHITAKER, J. S. & HAMILL, T. M. (2002). Ensemble data assimilation without perturbed observations. *Mon. Wea. Rev.*, **130**: 1913–1924.
- [56] <https://swot.jpl.nasa.gov/>